

Supporting Information

Atomic Co decorated free-standing graphene electrode assembly for efficient hydrogen peroxide production in acid

Zeheng Lin^{a+}, Qingran Zhang^{a+}, Jian Pan^{a*}, Constantine Tsounis^a, Ali Asghar Esmailpour^a, Shibo Xi^c,

Hui Ying Yang^d, Zhaojun Han^{a,b}, Jimmy Yun^{a,e,f}, Rose Amal^a, and Xunyu Lu^{a*}

- a. Particles and Catalysis Research Group, School of Chemical Engineering, The University of New South Wales, Sydney, NSW 2052, Australia.
- b. CSIRO Manufacturing, Lindfield, NSW 2070, Australia.
- c. Institute of Chemical & Engineering Sciences, Agency for Science, Technology and Research, 1 Pesek Road, 627833, Singapore.
- d. Pillar of Engineering Product Development, Singapore University of Technology and Design, 8 Somapah Road, 487372, Singapore.
- e. College of Chemical and Pharmaceutical Engineering, Hebei University of Science and Technology, Shijiazhuang, Hebei 050018, P. R. China
- f. Qingdao International Academician Park Research Institute, Qingdao, Shandong 266000, China

Corresponding authors: xunyu.lu@unsw.edu.au, jian.pan@unsw.edu.au

⁺These authors contributed equally.

Experimental section

Chemical and materials. Aniline ($\geq 99.5\%$), nitric acid 70%, potassium hexacyanocobaltate(III), perchloric acid 70%, Sulfuric acid (95%-98%, ACS agent), sodium phosphate dibasic ($\geq 99.0\%$), sodium phosphate monobasic ($\geq 99.0\%$), potassium hydroxide (99.99% trace metal basis), Nafion[™] perfluorinated resin solution (product code: 527084-25ML), PTFE emulsion (60%), methyl orange (MO), and potassium permanganate ($\geq 99.0\%$), were purchased from Sigma Aldrich. Toray carbon paper 090 (product code: 590337) and Nafion[™] 117 membrane were purchased from Fuel Cell Store. All (except the carbon paper) were used as received without further purification. Vertically aligned graphene (VG) was prepared in Commonwealth Scientific and Industrial Research Organization (CSIRO) following the previously reported procedures^{1,2}. The graphene products are also purchasable from the CSIRO official website (<https://research.csiro.au/graphene/service/buy-graphene-products>).

Electrode preparation. The preparation of CoN₄/VG electrodes from pristine VG can be briefly divided into three steps, polymerization, impregnation, and carbonization.

Prior to polymerization, the electrolyte was prepared according to the volume ratio of HNO₃: aniline: water = 16mL: 12mL: 150 mL. The electrolyte was freshly prepared for use every single time (50 mL). Then, a typical 3-electrode cell was established, consisting of VG substrate ($\sim 5 \times 5$ cm²) as working electrode, a graphite rod as a counter electrode, and a saturated calomel electrode (SCE) as a reference electrode. Aniline was electrochemically polymerized on the surface of VG by a potentiostatic method (0.7 V vs SCE, 100s) in the 3-electrode cell, and polyaniline on VG (denoted as PANI/VG) was derived as a result. After polymerization, the electrode was carefully washed with plentiful distilled water to remove the existed unstable polymerized components on the electrode surface, followed by drying at 80 °C for 1h. In a typical successful synthesis, the electrode was initially black and became deep green

when completely dried^{3, 4}. It should be noted here that extending the polymerization time has been considered in our work, but it induced nanofiber on top fully covering the VG network after the whole synthesis, which was reportedly unappealing for the rapid transfer process in the application (Figure S9)⁵. After that, the obtained optimized PANI/VG was inserted vertically into 0.149 g L⁻¹ K₃[Co(CN)₆] solution at 50 °C for 1 h under vigorous stirring (200 rpm) to introduce Co into the electrode. Then, the Co-absorbed polyaniline on VG electrode (denoted as Co/PANI/VG) was washed by distilled water again and dried at 50 °C this time before furnace carbonization. Carbonization process was performed using a tube furnace at 700 °C under N₂ atmosphere with a ramp rate of 5 °C min⁻¹ and this temperature was kept at 3h, followed by a room temperature acid wash procedure (0.5 M H₂SO₄ for 8 h) to afford the resultant CoN₄/VG, which was used for electrochemical evaluation in H-cell and the corresponding physical characterization. As a comparative sample, CoN₄/CP was fabricated following the same procedure as described above, so as the metal-free sample, NC/VG but in the absence of impregnation procedure. To note, the carbon paper before use should be heated to 700 °C to remove the impurity on the surface⁶⁻⁸. For the calculation of the active materials (Co-N-C) loaded in the resultant CoN₄/VG electrode, the weight change from pristine VG to the resultant was monitored accordingly with 1.9 mg increase for 25 cm² electrode, a typical figure that is measured in our multiple of preparation^{9, 10}. For a fair comparison, the same size of the pristine VG was also subjected to the 700 °C furnace treatment directly whose weight change was found negligible.

For the as-synthesized electrode being compatible in flow cell test, further electrode hydrophobic treatments are needed, following literature with minor modifications¹¹⁻¹⁵. To be specific: the electrode was exposed to 0.1% PTFE solution (diluted from 60% PTFE emulsion) for 10 mins, followed by a heat treatment (350 °C) in the tube furnace for 30 min under an argon atmosphere. After that, a certain

amount of Nafion[™] perfluorinated resin solution was sprayed onto the front side of electrode, resulting in the final CoN₄/VG based gas-diffusion electrode that was measured in the flow cell. CoN@CNTs electrode utilizing Co and N co-doped carbon nanotubes as catalyst was selected as the control same to confirm the facilitated mass transfer effect derived from the hierarchically porous structure of the CoN₄/VG electrode. It has a catalyst mass loading of 0.25 mg cm⁻² (cobalt loading : 20 μg cm⁻²) and the preparation follows the previous report¹⁶.

Electrode characterization. Field emission scanning electron microscopy (FE-SEM) was performed on FEI Nova Nano SEM 450 with high voltage of 5 kV for structural investigation or 15 kV in conjunction with Bruker SDD-EDS detector for compositional visualisation. Transmission electron microscopy (TEM) was carried out on a Phillips CM200 microscope at an accelerating voltage of 200 kV. X-ray diffraction (XRD) patterns were collected from thin-film Empyrean X-ray diffractometer using Cu K α radiation with 45 kV and 20 mA applied. High-angle annular dark field-scanning transmission electron microscopy (HAADF-STEM) and energy dispersive X-ray (EDX) mapping were obtained on a spherical aberration corrected transmission electron microscope (JEOL JEM-ARM200F) operating at 200 kV. For electrode compositional and electrolyte analysis, inductively coupled plasma mass spectrometry (ICP-MS) was performed on PerkinElmer quadrupole Nexion instrument. Prior to ICP-MS measurement, the samples were extracted with aqua regia deriving the digests for analysis. X-ray photoelectron spectroscopy (XPS) was also used to understand the chemical compositions of as-prepared electrodes with ESCALAB250Xi X-ray photoelectron spectrometer.

Co K-edge X-ray absorption near-edge spectroscopy (XANES) measurements and Extended X-ray absorption fine structure (EXAFS) experiments were performed at the XAFCA beamline of Singapore

Synchrotron Light Source (Singapore Synchrotron) with Co foil, CoO, and CoPc as the reference samples. Data reduction and subsequent simulation efforts were performed using the Athena program and the Artemis program, respectively. To perform the fitting analysis of CoN₄/VG, the k-space ranging from 3 Å⁻¹ to 7.5 Å⁻¹ is collected and the R range is adopted within 1 Å to 2.2 Å. Firstly, the amplitude reduction factor S₀² (0.74000) is confirmed by fitting the EXAFS signal of the cobalt foil. As for the fitting of the Co edge data for CoN₄/VG, a standard single-crystal cobalt phthalocyanine (C₃₂H₁₆CoN₈ molecular) structure from crystallography (2100746, link: <http://www.crystallography.net/cod/2100746.html>) was adopted as the atomic model. The parameters of delE (edge-energy shift) and S₀² were fixed, while CN (coordination numbers), delR (the change of the interatomic distance relative to the initial path length), and σ² (Debye-Waller factor), were allowed to run freely.

Electrochemical measurements. All electrochemical measurements were performed in 0.1 M HClO₄ (except the feasibility demonstration in 0.1 M PBS and 0.1 M KOH) at 25 °C using a CHI750 electrochemical workstation without compensating any Ohmic resistance of the systems (H cells and flow cells). The pH value of 0.1 M HClO₄, 0.1 M PBS, and 0.1 M KOH were measured as 0.99, 6.8, and 13.1 respectively, by Metrohm pH meter 913.

To evaluate the performance of electrodes in H-cell (Gaoss Union), a standard three-electrode system was established with a graphite rod (Sigma Aldrich) and a saturated calomel electrode (CHI 150, SCE) respectively as the counter electrode and the reference electrode, in which SCE was calibrated regularly during the period of data collection. All the measured potentials were then converted to RHE (reversible hydrogen electrode) following the Nernst equation of $E_{\text{RHE}} = E_{\text{SCE}} + 0.2415 + 0.059 \times \text{pH}$. For background current (non-faradaic current) measurement, the electrolyte was firstly saturated with

N₂ gas, and then linear sweep voltammetry (LSV) was performed several times at a scan rate of 5 mV s⁻¹ within the potential range of 0.3V to 0.8V vs RHE until a stable LSV response was established in H-cell. To assess the electrocatalytic ORR performance, LSV was carried out again following the same protocol but the electrolyte was saturated with O₂ this time. H₂O₂ selectivity of the as-synthesized electrodes was evaluated by applying chronoamperometry technique at each working potential for 1 h and was repeated for 3 times, with fixed amount of oxygen-saturated catholyte (40 mL) being refreshed before each test. Chemical titration with KMnO₄ was adopted to quantify the amount of H₂O₂, following the previous reports¹⁷⁻¹⁹. Then, the H₂O₂ selectivity (faradaic efficiency, FE) was calculated based on the following equation: $H_2O_2 \text{ (Fe, \%)} = 2CVF/Q$ Where Q represents the charge amount (C) recorded by CHI 750 workstation, C is the produced H₂O₂ concentration (mol L⁻¹) derived from titration, V is the volume of catholyte (L) and F is the value of faraday constant (96485 C mol⁻¹). For bulk electrosynthesis, the electrode (~2 cm²_{geo}) was used directly, with oxygen continuously (15 mL min⁻¹) bubbling the catholyte (40 mL) under vigorous stirring (800 rpm). After each synthesis, the concentration of H₂O₂ in the electrolyte and the corresponding productivity were measured accordingly. It should be noted that the productivity (normalized production rate to the mass (in H-cell and flow cell) or to the geometric surface area (in flow cell only)) is an important metric used to reflect the intrinsic catalytic performance of the catalyst materials for H₂O₂ electro-synthesis, which also has been widely adopted in previous report^{20, 21}. This metric is calculated based on the actual mass of hydrogen peroxide (mg) accumulated over the long-term operation to per gram of catalyst materials. The in-situ Raman spectra under ORR condition of CoN₄/VG were performed on a Renishaw inVia 2 spectrometer with a laser of λ=532nm, in conjunction with a custom-made Raman cell that allows Raman signals to go through the electrolyte and be collected. To estimate the electrochemical surface

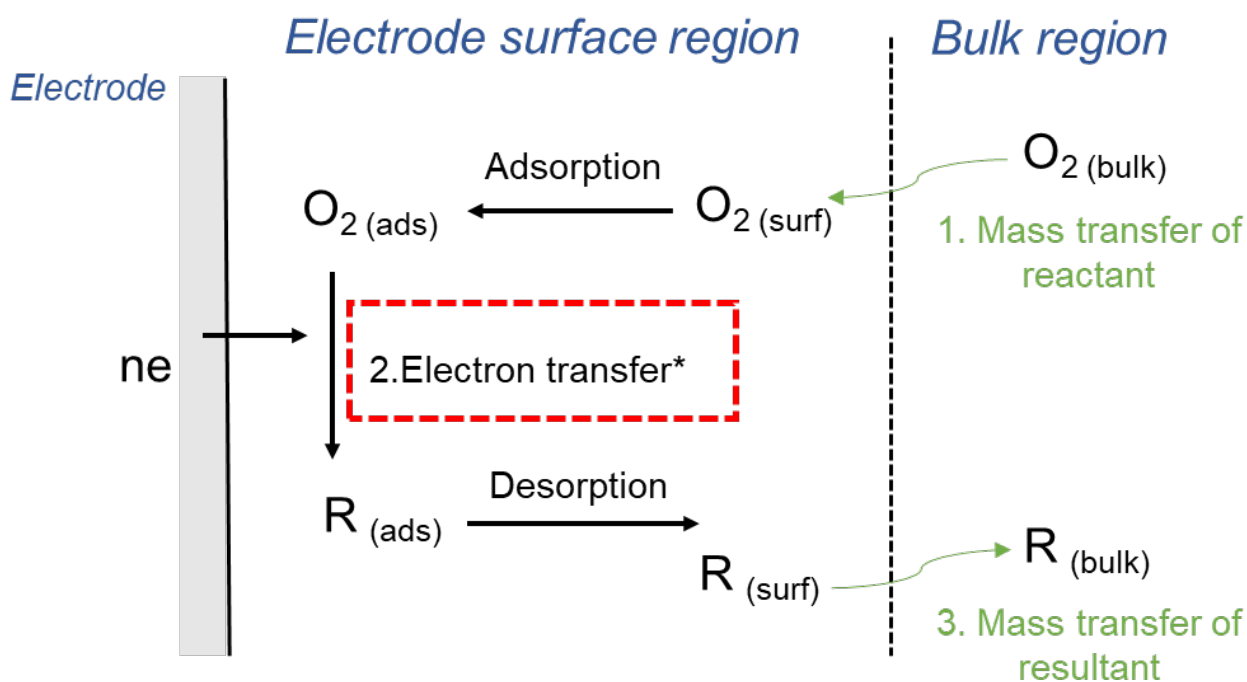
area (ECSA), the CV at a scan rate of 10, 20, 50, 80 and 100 mV s⁻¹ was recorded in the non-faradaic region (0.7 V vs SCE to 0.9 V vs SCE) in the inert gas-saturated (N₂) electrolyte to determine the double layer capacitance (C_{dl}) that is proportional to ECSA. The 2e⁻ ORR mechanism study was performed by virtue of rotation disk electrode technique (RDE), following the previously report strategy^{22, 23}. To prepare the electrode for RDE measurement, the CoN₄/VG was punched into a regular shape with the same size of the glassy carbon disk (S = 0.196 cm²) on RDE and then immobilized on its surface. It should be noted that the catalytic ORR current densities obtained from CoN₄/VG-loaded RDE could exceed the theoretical limited value estimated by Levich equation (3 mA cm⁻² in oxygen saturated 0.1 M HClO₄ under a rotating speed of 1600 rpm for 2e⁻ ORR)²³⁻²⁵. This is mainly ascribed to the as-fabricated 3D porous architecture on CoN₄/VG, which will inevitably promote a faster mass transport of reactants than that of conventional thin-film RDE employing the powdery catalysts. Therefore, the Levich equation may not be suitable to determine the theoretical limited ORR current density on our electrodes. Given this fact, an alternative way, taking the current density value at 0.2 V_{RHE} as the diffusion-limited current density (J_l), was adopted for further calculation of kinetic current densities (J_k) and the corresponding Tafel analysis^{20, 21}. The number of electron transferred (n) during ORR was calculated from the Koutecky–Levich (K–L) plots on the basis of the K–L equations accordingly, as followed: $i^{-1} = i_k^{-1} + i_l^{-1} = i_k^{-1} + \frac{1}{0.2nFAC_0D_0^{2/3}v^{-1/6}\omega^{1/2}}$, and Slope = $\frac{1}{0.2nFAC_0D_0^{2/3}v^{-1/6}}$ where F was the Faraday constant (96500 C mol⁻¹), A is the disk surface area (0.196 cm²), v is the kinematic viscosity (0.01 cm² s⁻¹), C₀ is the concentration of oxygen in 0.1M HClO₄ (0.00126 mol L⁻¹) and ω is the rotation speed of the electrode (rpm), while the D₀ is the diffusion coefficient of O₂ (0.000017 cm²s⁻¹).

The cell performance of CoN₄ /VG was carried out in a commercially available Micro flow cell (MFC,

Electrocell North America). This H₂O₂ flow cell comprises a cathode and an anode with three chambers (two liquid chambers and one feeding gas chamber). On the anode side, a dimensionally stable anode (iridium/ruthenium-coated titanium mesh, 10 cm²_{geo}) was served as the anode (oxygen evolution reaction, OER) installed on the anode chamber, in close contact with NafionTM 117 membrane to minimise the ohmic resistance loss during operation (~3.2 Ohmic was recorded if around 1 cm distance between anode and membrane). 0.1 M HClO₄ was circulated through the anode chamber during operation (90 mL h⁻¹). As for the cathode part, modified CoN₄/VG based gas-diffusion electrode (10 cm²_{geo}) worked as the cathode sandwiched between the liquid chamber and the gas chamber, with gas (15 mL min⁻¹) feeding on the macroporous side (backside of the electrode) from the gas chamber in a flow by configuration to mitigate the limited dissolvability of O₂ (40 mg L⁻¹ at 1atm, 25 °C), as well as its low diffusion coefficient (2.1 × 10⁻⁵ cm² s⁻¹ in water) in the liquid phase. In a similar flow by manner, the fresh electrolytes were pumped into the liquid chamber (with a flow rate of 90 mL h⁻¹), through the catalyst surface (frontside of the electrode) and finally carried out the resultant H₂O₂ for subsequent environmental treatments or analysis (electrolyte single-pass mode). To note, higher concentration of H₂O₂ can be harvested in our electrolyser (up to 2000 ppm at the voltage of 1.8V within 1 hour) by simply switching to electrolyte circulating mode (30 mL). Furthermore, the system Ohmic resistance in 0.1 M HClO₄ was measured via high-frequency AC impedance technique as ~1.6 Ohmic but no compensation was presented. The energy consumption (Wh g_{H2O2}⁻¹) was calculated by the following equation²⁶: Energy consumption = 1000*UIt*/*CV* Where *U* and *I* respectively represent the applied cell voltage (V) and current (A), *t* is the electrolysis time (h), *C* is the concentration of as-produced hydrogen peroxide (mg L⁻¹), and *V* is the electrolyte volume (L). The calculation of Turnover number (TON) is based on the equation: TON =

number of H₂O₂ molecules produced / the amount of moles of cobalt . The production of H₂O₂ was determined by titration, while the cobalt amount on the catalyst was determined through ICP-MS. After that, turnover frequency (TOF) is calculated by the equation : $TOF = TON / \text{time of reaction}(h)$.

Degradation of a typical refractory organic pollutant. For the Fenton process, H₂O₂ produced from bulk electrosynthesis was used (1100 ppm) with the addition of 0.5 mM Fe²⁺, together to degrade methyl orange (50 mg L⁻¹). The electro-Fenton reaction was performed in a custom-made reactor (40 mL) using CoN₄/VG (~2 cm²_{geo}) as the working electrode, with the same Fenton reagent as the electrolyte. This process was operated at 0.3 V vs RHE. The concentration evolution of methyl orange during degradation was measured by UV-VIS (UV-3600 plus, Shimadzu).



R: H₂O₂ or H₂O

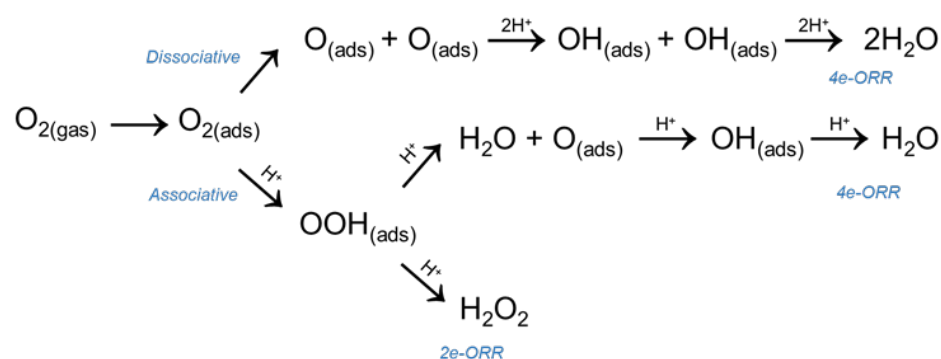
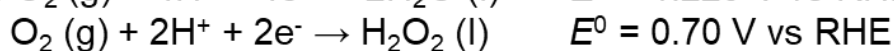


Figure S1. Electrochemical process of oxygen reduction electrode reaction (ORR) in acidic media²⁷.

This process generally composes a series of steps including mass transfer, electron transfer at the electrode surface, chemical reactions coupled to electron transfer and surface reactions such as adsorption or desorption. Electron transfer is usually kinetically unfavourable as energy is required for the cleave of O-O bond, but reactant transfer step can count equally or more while increasing applied potential to seek higher H₂O₂ productivity in the application. Mass transfer of the resultant step does not directly determine the reaction rate; however, a sluggish acidic peroxide removal rate from the Supporting information page 10

electrode surface can cause local peroxide accumulation. Accumulated peroxide ends up either further electrochemical reduction (H_2O_2 to H_2O) or giving rise to electrode failure caused by the strong oxidant of locally concentrated acidic peroxide. Both would substantially reduce productivity, and hence a well-round electrode design is needed based on the electrochemical process of ORR.

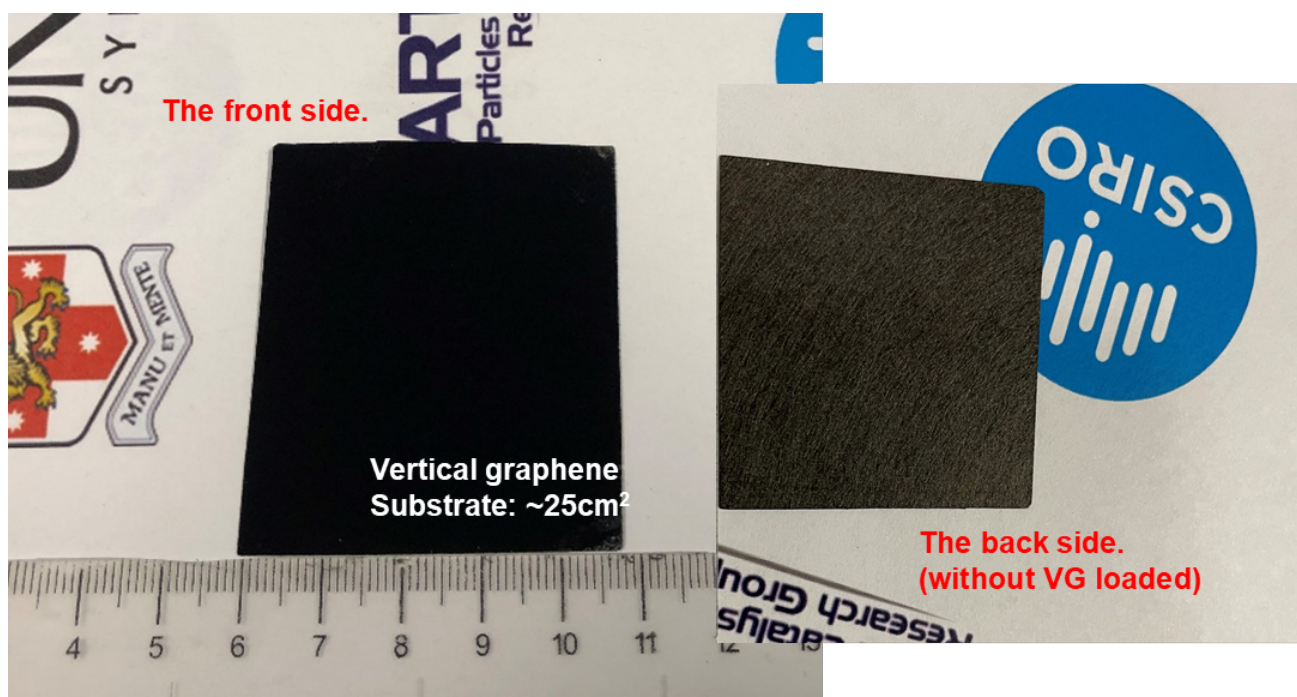


Figure S2. Digital photo of a typical as-prepared vertical graphene ($\sim 25 \text{ cm}^2$) that can be compatible with most of the commercially available electrolysers.

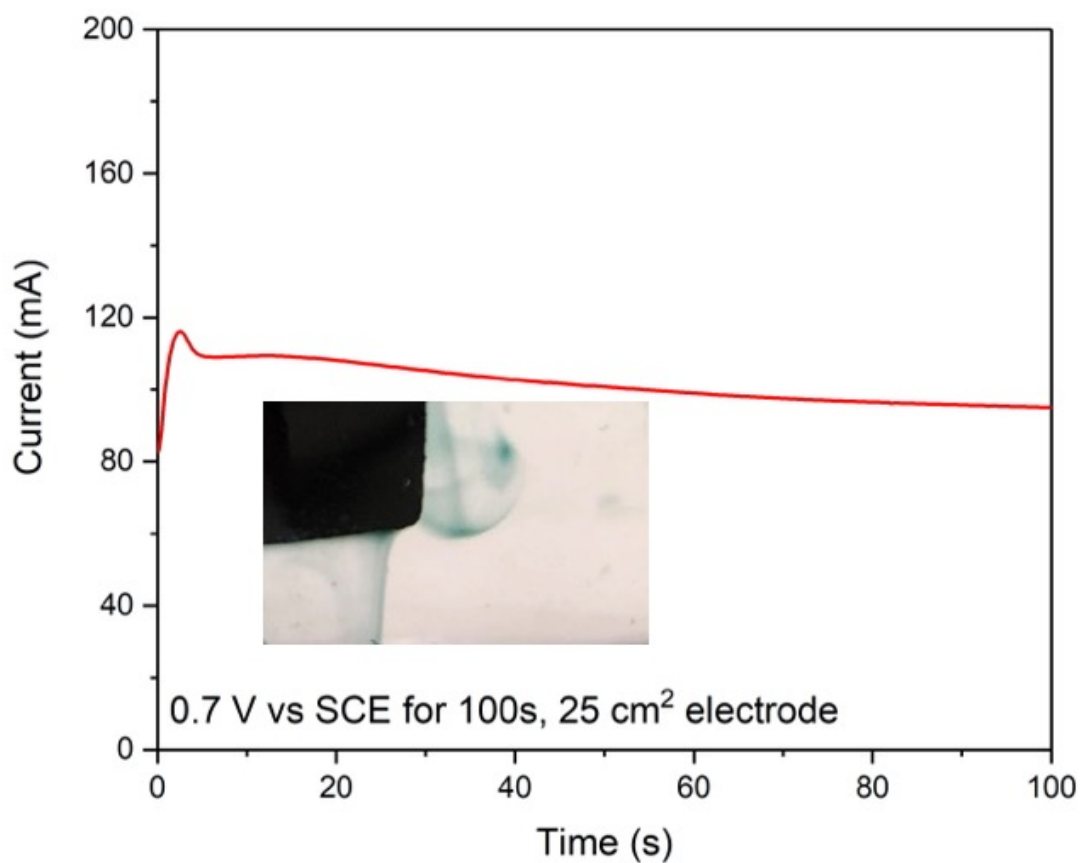


Figure S3. Current-time response signal record at applied potential of 0.7 V vs SCE with vertical graphene as working electrode during 100s polymerization, showing a stable current response, an indicative of the uniform deposition of polyaniline on the vertical graphene surface, which is further confirmed by the SEM image in main text (Figure 1b).

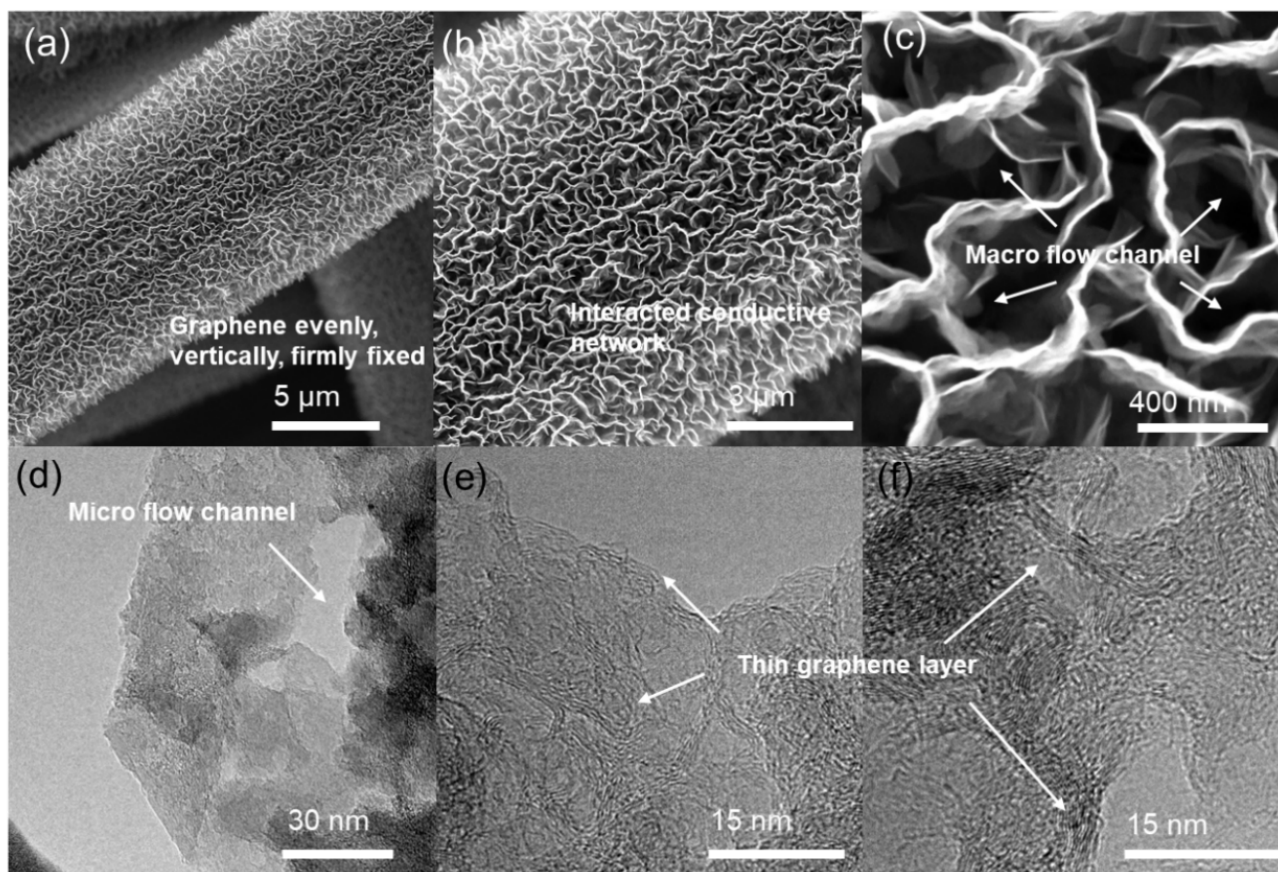


Figure S4. SEM images (a, b, and c) and TEM images (d, e, and f) of the as-prepared vertical graphene (VG) substrate showing its multistage porous, vertical align nature, which could be beneficial for CoN_4 moieties enabling rapid electrode process.

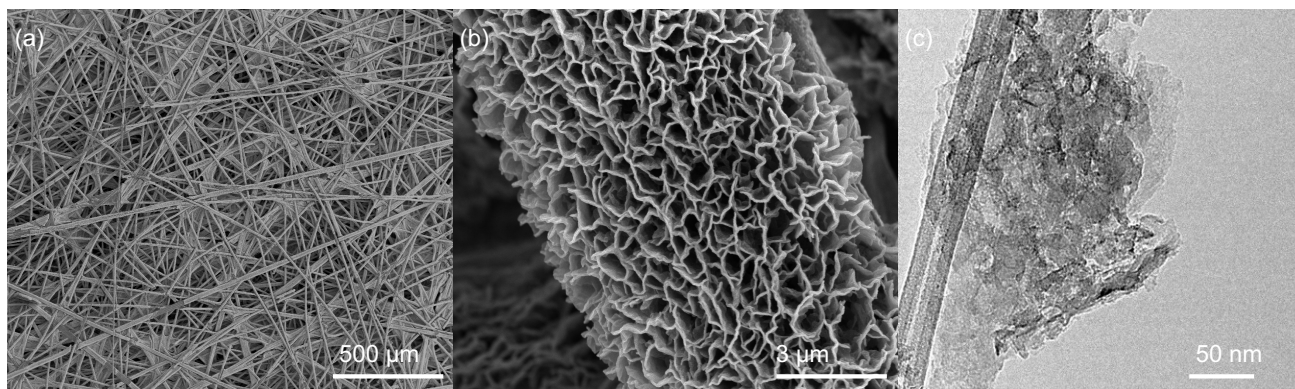


Figure S5. SEM images (a and b), and TEM image (c) of the resultant CoN₄/VG electrode.

it is clear that the catalyst electrode consists of a hierarchical porous structure, including those macroporous channels inherited from the carbon fibre paper (Figure S5a), the open-end pores created by the vertical graphene nanoarrays (Figure S5b), and numerous mesopores on each CoN₄-loaded VG nanosheets (Figure S5c). Benefited from such a hierarchically porous structure, the as-obtained CoN₄/VG electrode can facilitate the exposure of more catalytically active sites, an enhanced mass transport, and thereby an effectively accelerated ORR process for H₂O₂ generation.

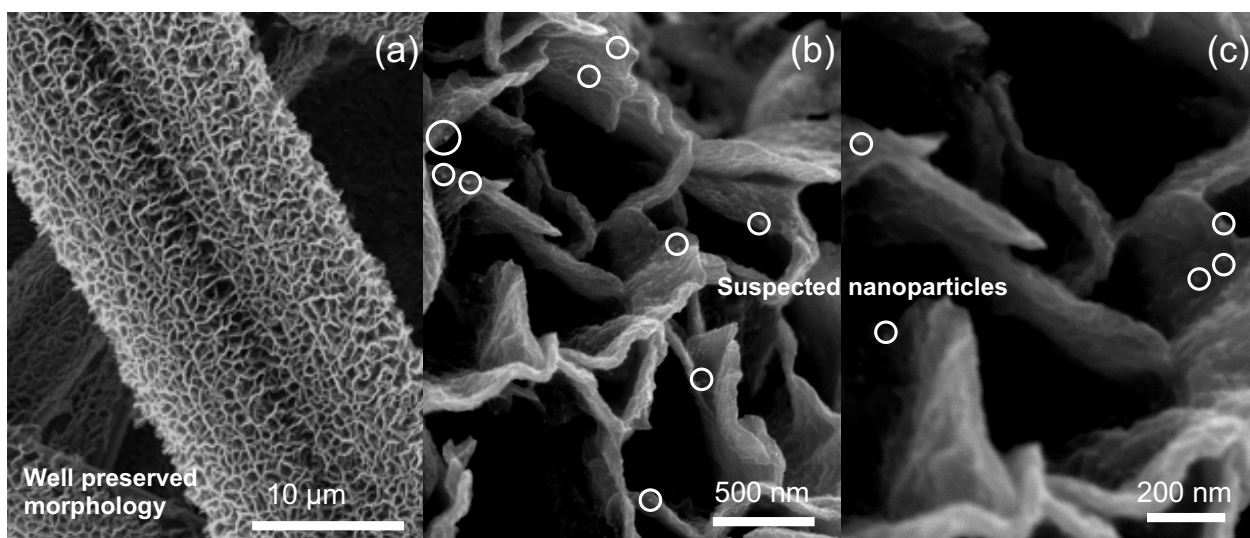


Figure S6. SEM images of the as-synthesized electrode (CoN_4/VG prior acid wash) without acid wash at different magnifications (a, b, and c), showing some suspected nanoparticles encapsulated but the well maintained microstructure.

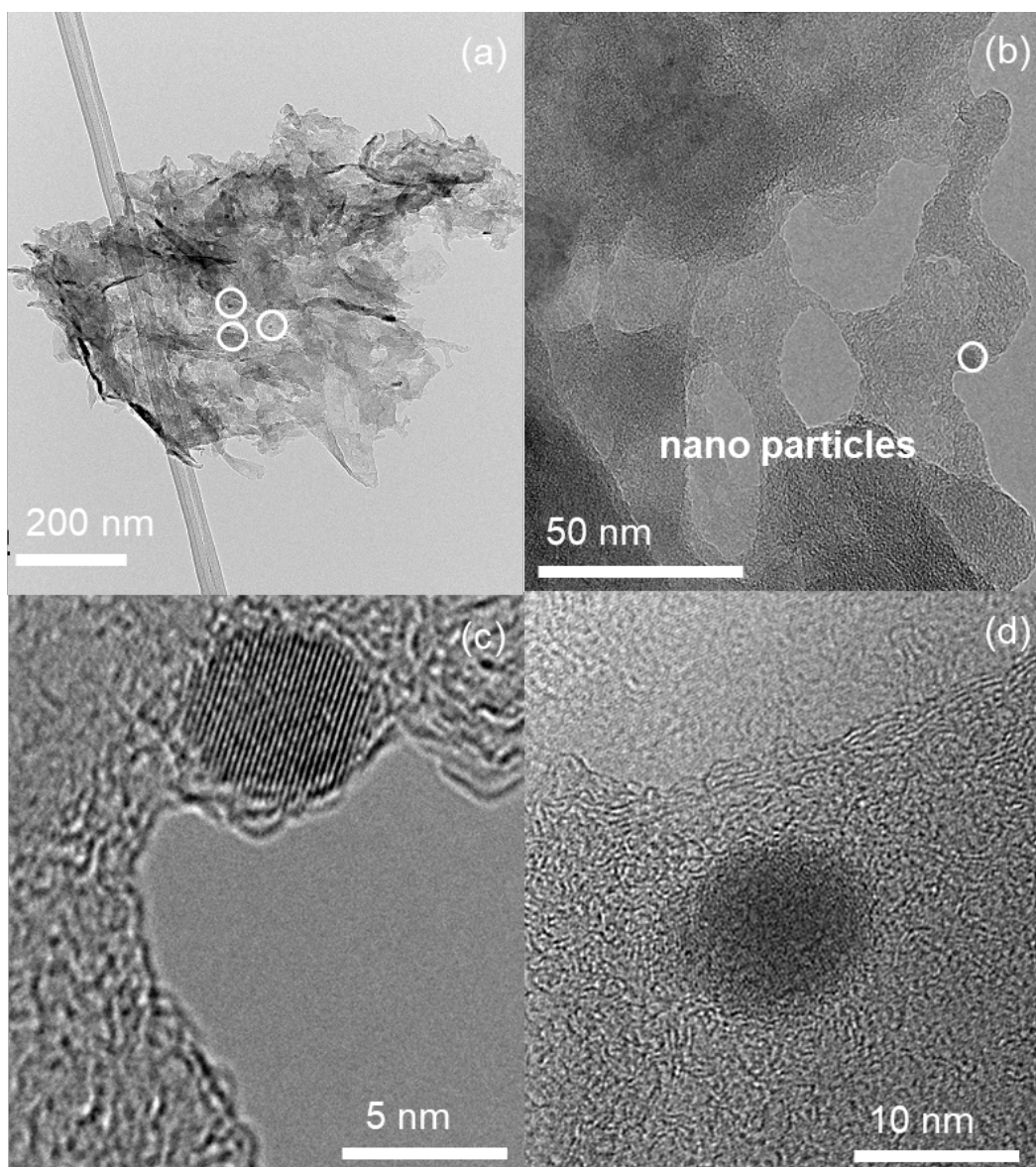


Figure S7. TEM images of the as-synthesized electrode without acid wash (CoN₄/VG prior acid wash), showing the presence of some nano particles.

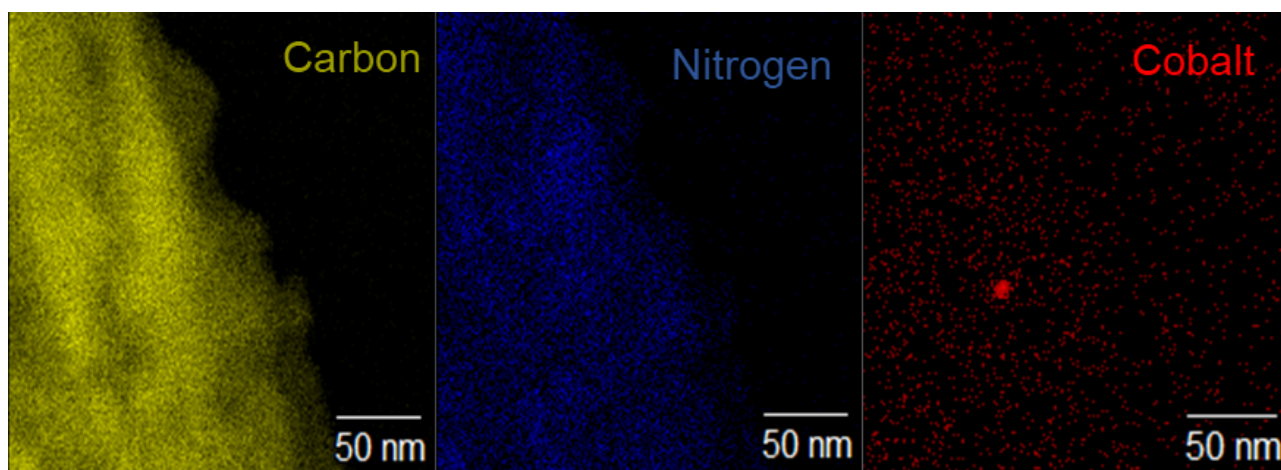


Figure S8. TEM EDS mapping of as-synthesized electrode without acid wash (CoN_4/VG prior acid wash) showing the dense cobalt signal from the presented nano particle.

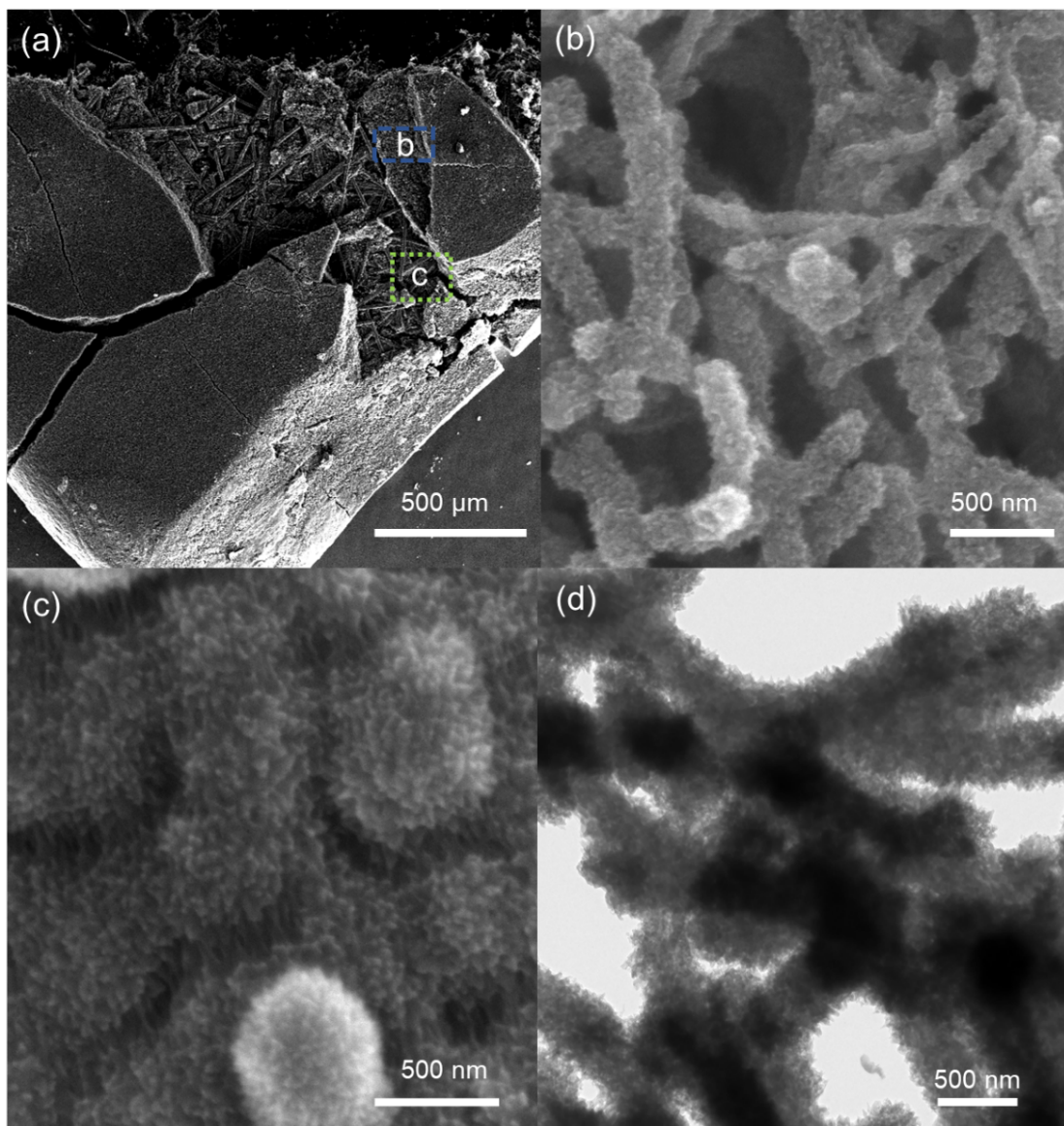


Figure S9. SEM images of PANI/VG electrode using a typical excessive polymerization time of 500s (a), with enlarged images showing details (b and c), and the corresponding TEM image (d).

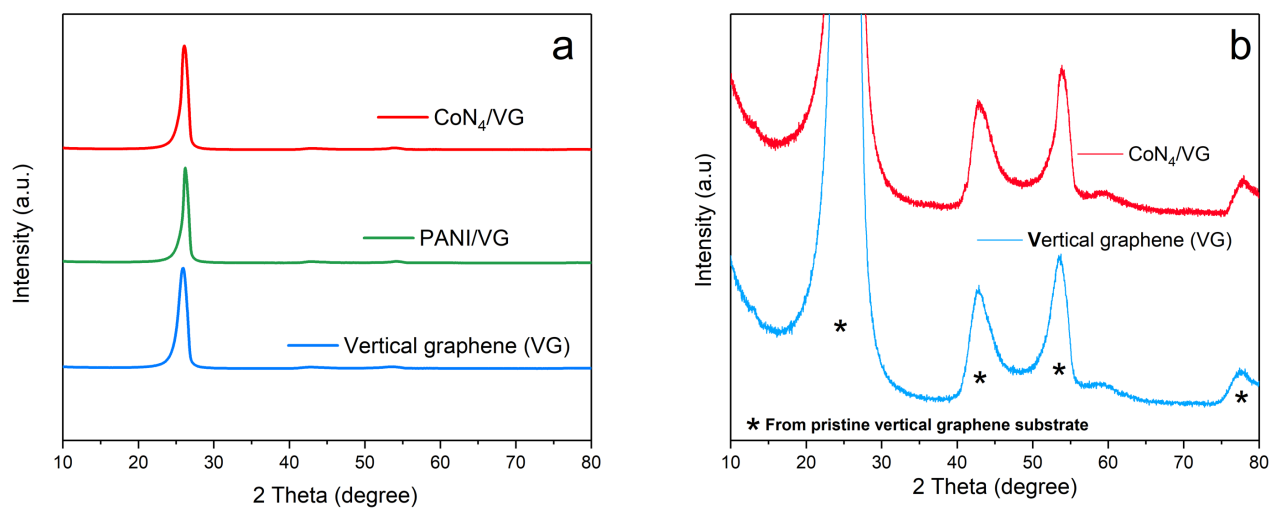


Figure S10. XRD patterns of CoN₄/VG electrode, polyaniline on VG (PANI/VG), and pristine VG substrate (a); Enlarged XRD patterns of CoN₄/VG electrode and pristine VG (b). The results here show that no obvious characteristic peaks attributed to metallic species can be observed from the diffraction pattern of CoN₄/VG electrode.

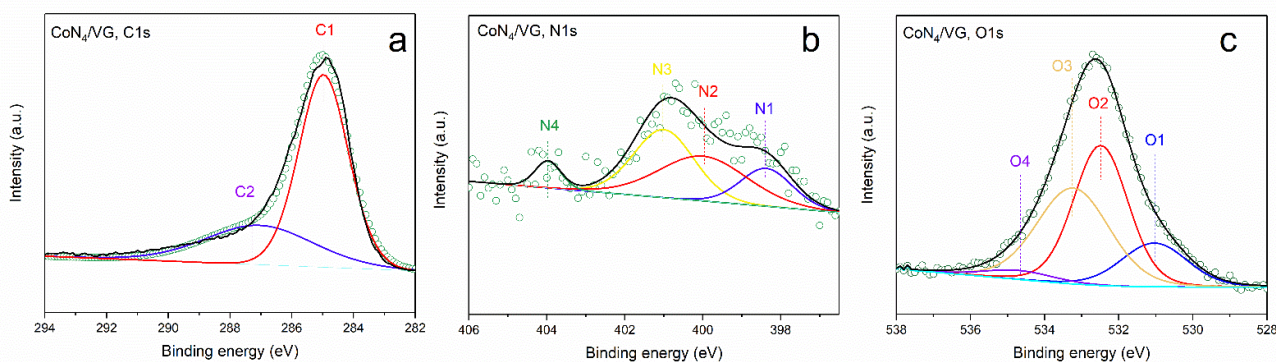


Figure S11. XPS C 1s spectrum of the resultant CoN₄/VG electrode, showing carbon species including C=C (C1), at ~284.9 eV and C-O (C2) at ~287.4 eV (a)^{28, 29}; N 1s spectrum, showing nitrogen species including pyridinic nitrogen (N1) at ~398.4 eV, pyrrolic nitrogen (N2) at ~399.9 eV, graphitic nitrogen (N3) at ~401 eV, and N-oxide (N4) at ~404 eV (b)³⁰; and O 1s spectrum, showing the oxygen species including ketonic oxygen (C=O, O1, ~531.2 eV), oxygen atoms in epoxy (C-O-C) or hydroxyl groups and carbonyl oxygen in ester groups (O2, ~532.3 eV), the epoxy oxygen in ester groups (O3, ~533.5 eV), and oxygen atoms in carboxyl groups (O4, ~534.2 eV) (c)³¹.

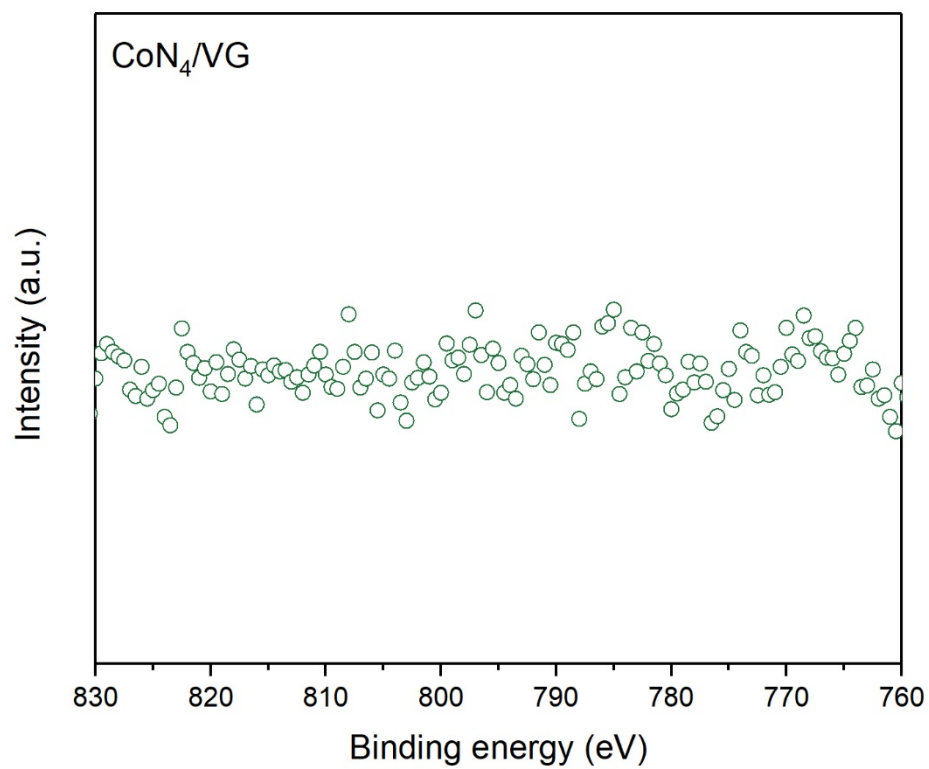


Figure S12. XPS Co 2p spectrum of the resultant CoN₄/VG electrode.

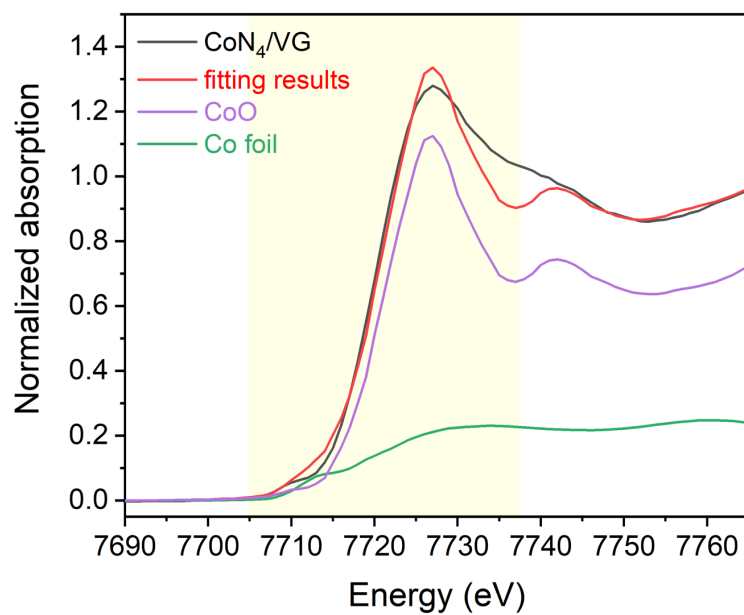


Figure S13. LCF results for Co K-edge XANES normalized spectra of the CoN₄/VG electrode from the interaction of CoO and Co foil. The fitted range of Co K-edge XANES spectra of CoN₄/VG was highlighted with a yellow square window.

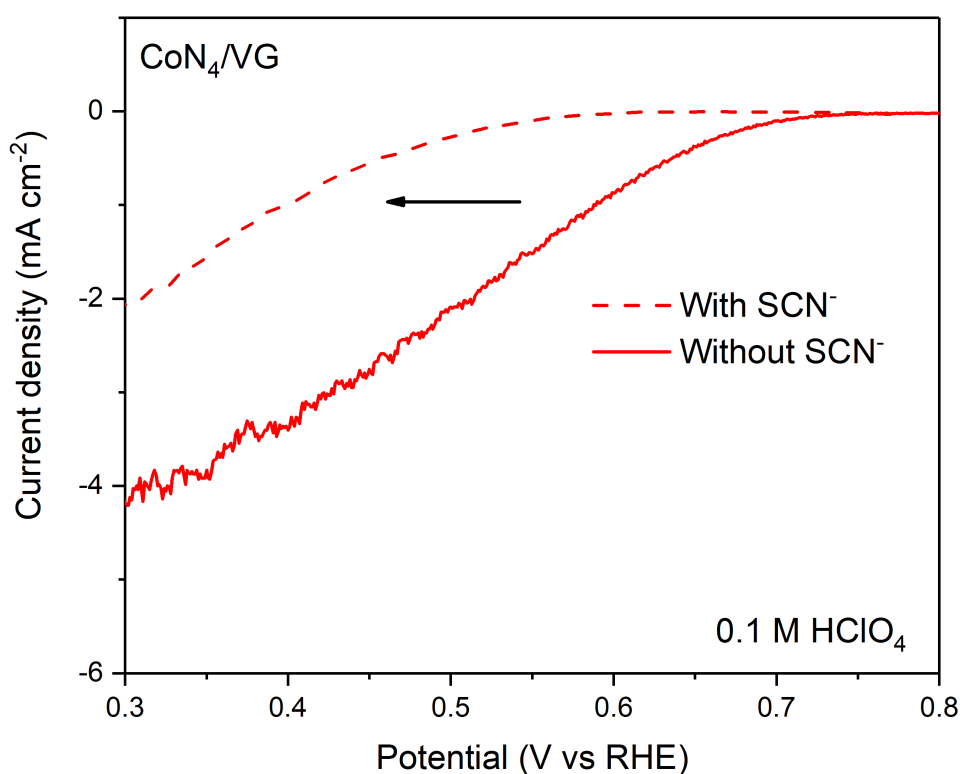


Figure S14. Poison experiment of CoN₄/VG electrode before and after introducing KSCN solution under the ORR condition in 0.1 M HClO₄ with a scan rate of 5 mV s⁻¹, which indicates the typical catalytic active decrease of CoN₄ after introducing KSCN.

In order to understand the nature of the active sites of CoN₄/VG electrode, the influence of thiocyanate ions (SCN⁻) on the ORR activity was investigated. SCN⁻ is reported to be effective in poisoning the metal-centered catalytic sites in acidic media, according to the previous reports^{32, 33}. In our system, after 10 mM SCN⁻ was introduced into 0.1 M HClO₄ electrolyte, the CoN₄/VG electrode shows substantially decreased catalytic activity, indicating the main role of Co-N site on the as-synthesized electrode as the catalytic active center.

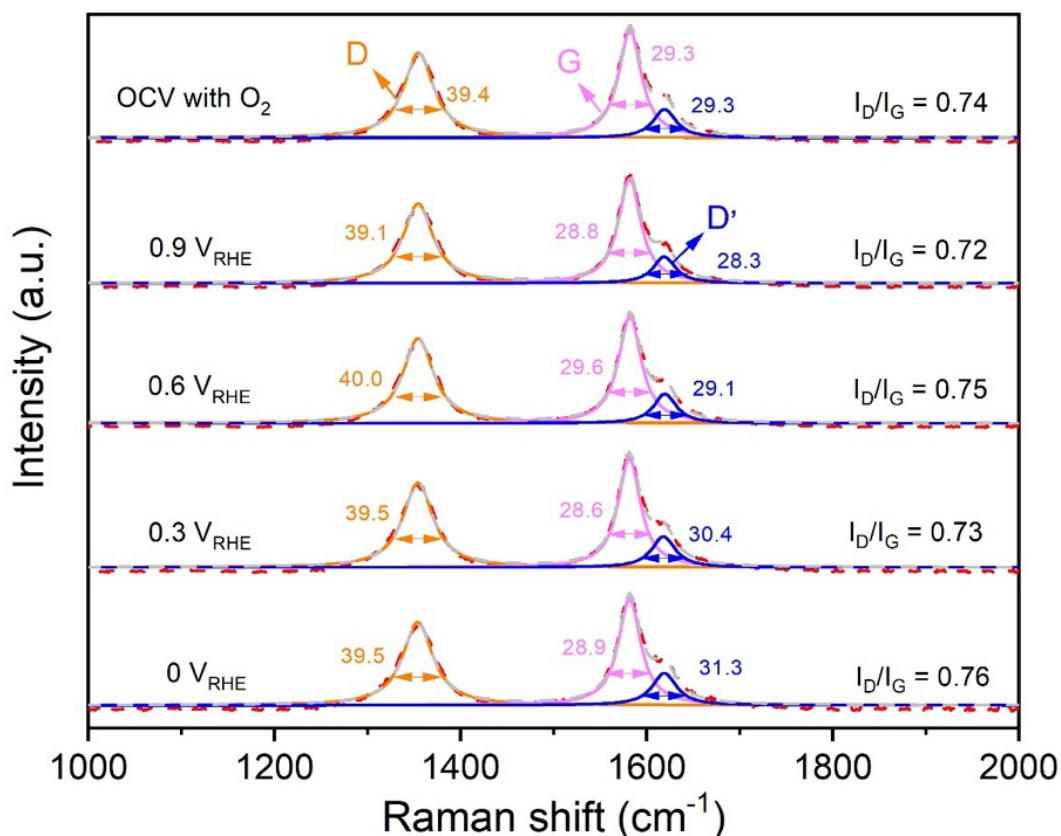


Figure S15. In-situ Raman spectra-with calculated Lorentz deconvolutions-of CoN₄/VG under various applied potentials. O₂-saturated 0.1 M HClO₄ was used as the electrolyte throughout the tests.

in-situ spectroscopic analysis was also carried out through Raman measurements under the ORR conditions. As expected, Raman spectra of CoN₄/VG (Figure S15) reveals three characteristic peaks of a disordered carbon nanostructure due to heteroatom doping, which are the G band (~1580 cm⁻¹), D band (~1350 cm⁻¹) and D' band (~1620 cm⁻¹). Notably, previous reports suggest a significant change on the full width at half peak maximum (FWHM) of D and D' bands during reaction if the carbon defects (e.g. sp³ disorder reflected by D band) or surface oxygen functionalities (e.g. carbon oxidation in sp² basal plane reflected by D' peak) are the main active sites, which tend to interact with ORR intermediates.^{29, 34} Nevertheless, in this study, no obvious changes (<2) can be observed on the FWHM of D and D' bands at both low and high overpotential ranges (Figure S15), in sharp contrast to those defective carbon catalysts showing a huge variation (above 10).²⁹ In this regard, the possible

contribution from the carbon and/or oxygen defects on CoN₄/VG electrode for the ORR process can be further excluded, supporting the chemical poisoning experiments that the superior 2e⁻ ORR activity is mainly originated from the as-deposited CoN₄ species. Moreover, the nearly constant I_D/I_G value (~0.74±0.02) on the CoN₄/VG catalysts throughout the ORR process further confirms a stable property of carbon skeleton during reaction, in conformity with other post-reaction characterizations (e.g. SEM, TEM, XRD and XPS). Therefore, combined ex-situ and in-situ analysis indicates that CoN₄/VG is stable under the ORR conditions, and the CoN₄ species are the main active moieties.

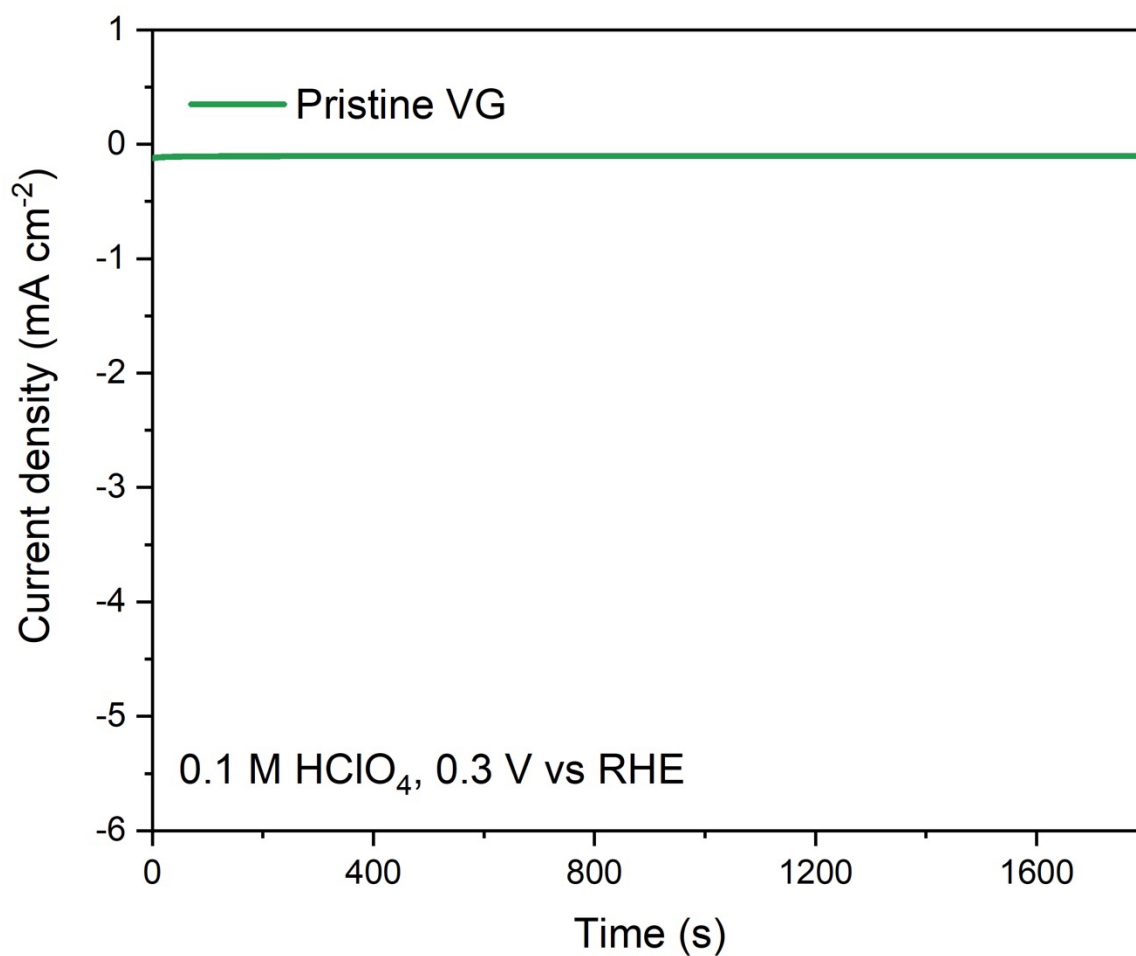


Figure S16. I-T curve of pristine VG electrode (2cm²) in H-cell at 0.3 V vs RHE within 1800s, showing negligible ORR performance as compared with that of CoN₄/VG electrode.

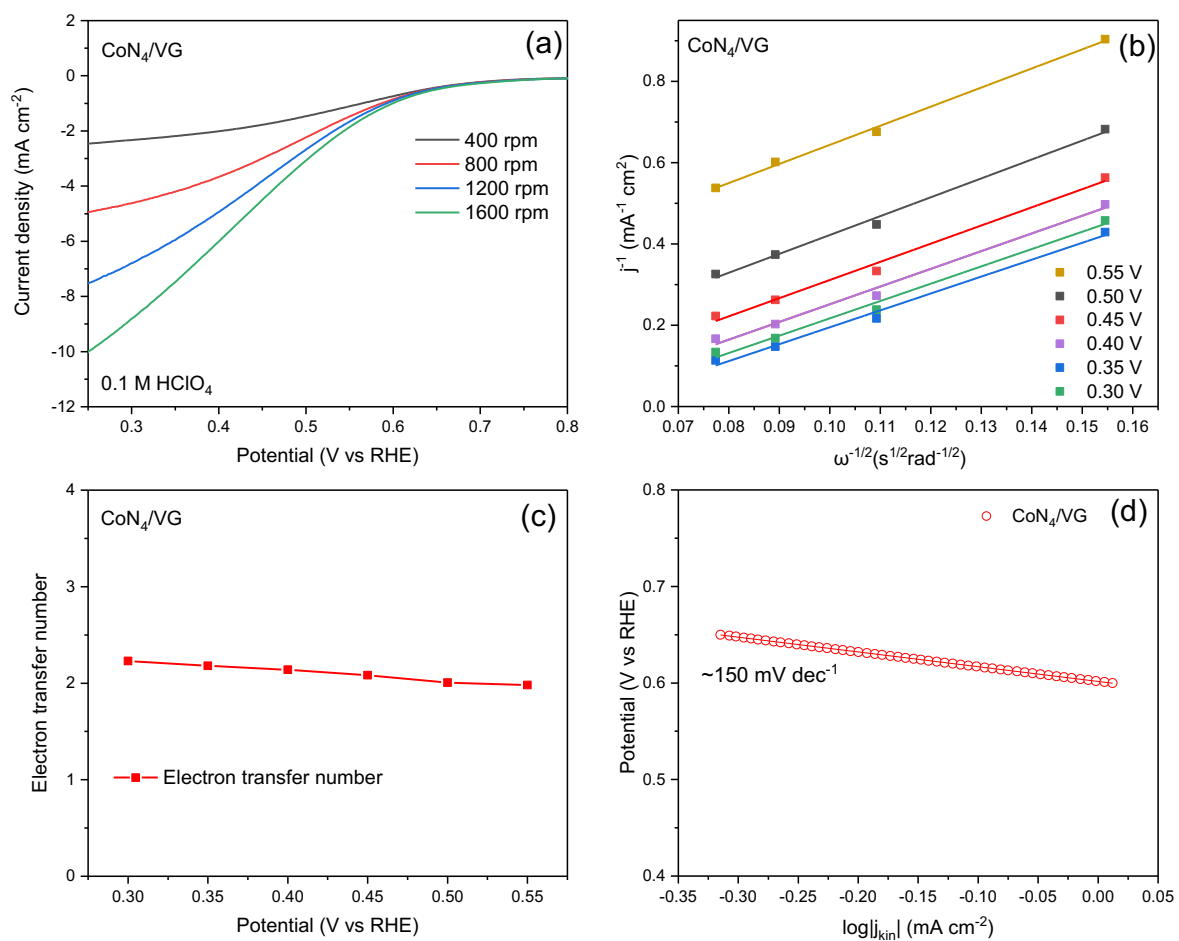


Figure S17. RDE voltammograms of CoN₄/VG at different rotation speeds (a), K-L plots of CoN₄/VG at the selected voltages (b), and their calculated electron transfer number (c), and Tafel plot of CoN₄/VG derived from the kinetic current densities (d).

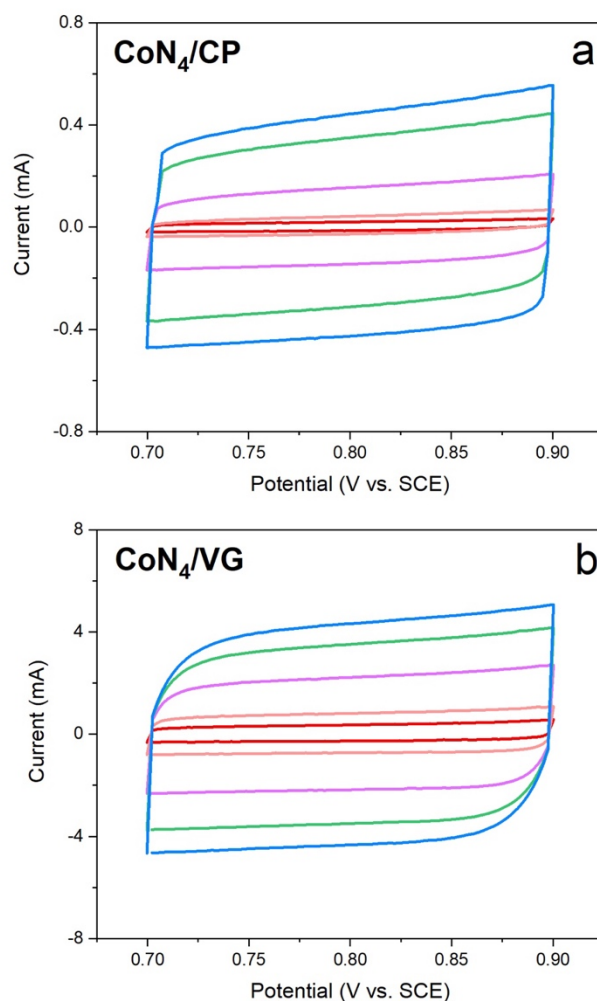


Figure S18. Charging and discharging currents measured in the non-Faradaic potential range (0.7 V vs SCE to 0.9 V vs SCE) at scan rates of 10, 20, 50, 80, and 100 mV s^{-1} with the CoN_4/CP electrode (a) and the CoN_4/VG electrode (b) in 0.1 M HClO_4 solution (the electrolyte was saturated with N_2 before test).

The electrochemically active surface area (ECSA) can represent the area of an electrode that is accessible to the electrolyte and could be used for the charge transfer.³⁵ The ECSA is proportional to the electrochemical double-layer capacitance, which can be measured by cyclic voltammetry (CV) in a potential window where Faradaic process is considered to be negligible. Accordingly, the double-layer capacitance (C_{dl}) is then evaluated to estimate the electrochemical active surface area (ECSA) of each electrode (Figure S18 and Figure S19).

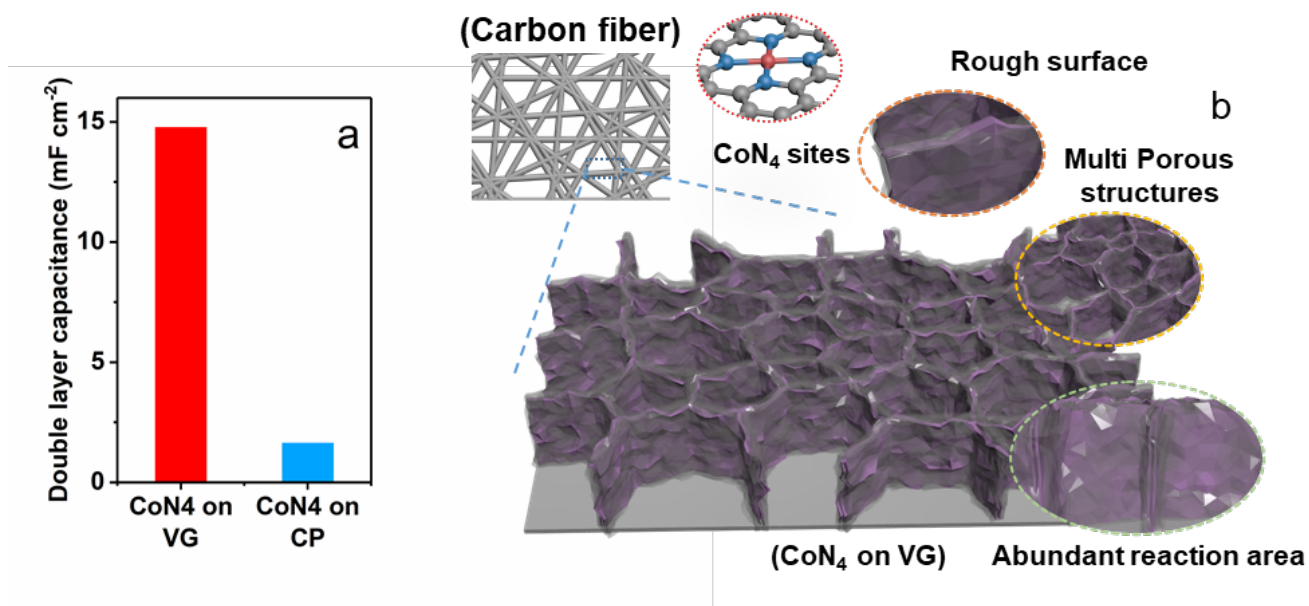


Figure S19. Double-layer capacitance of the CoN₄/VG electrode and the CoN₄/CP electrode (a); Illustration of the benefits of utilizing VG for CoN₄ giving a high electrochemical active surface area (b).

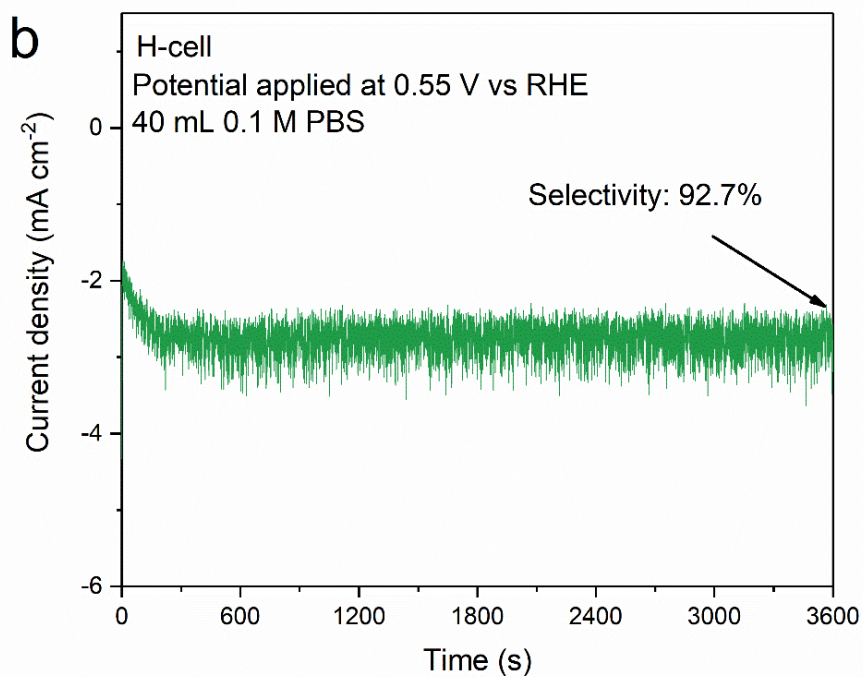
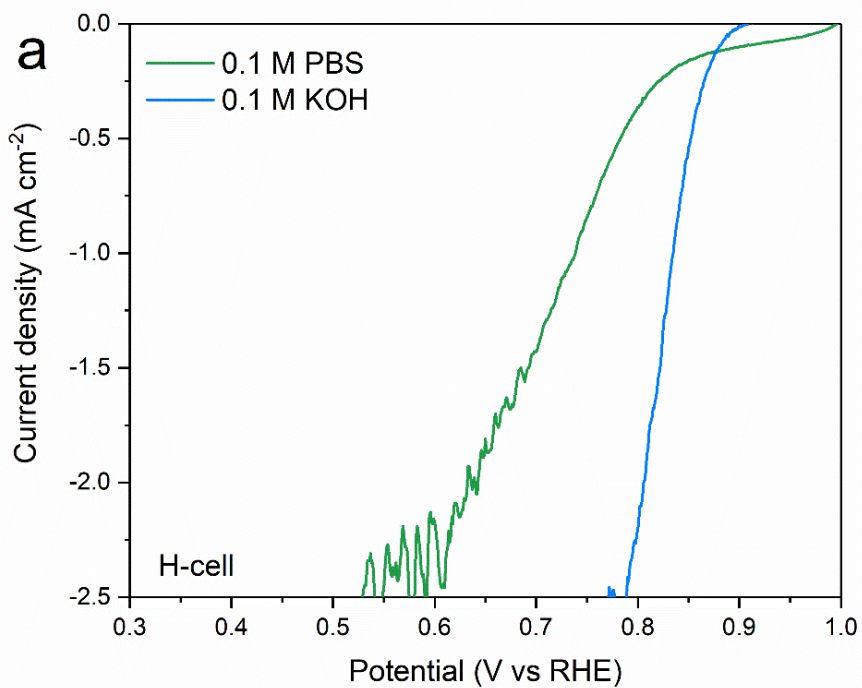


Figure S20. Linear sweep voltammetry (LSV) curve of CoN₄/VG electrode with 5 mV s⁻¹ scan rate in 0.1 M PBS and 0.1 M KOH electrolytes (a); I-T curve of CoN₄/VG electrode at 0.55 V vs RHE in H-cell within 3600s (40 mL electrolyte, electrode size: 2cm²), with 92.7% of 2e⁻ ORR selectivity.

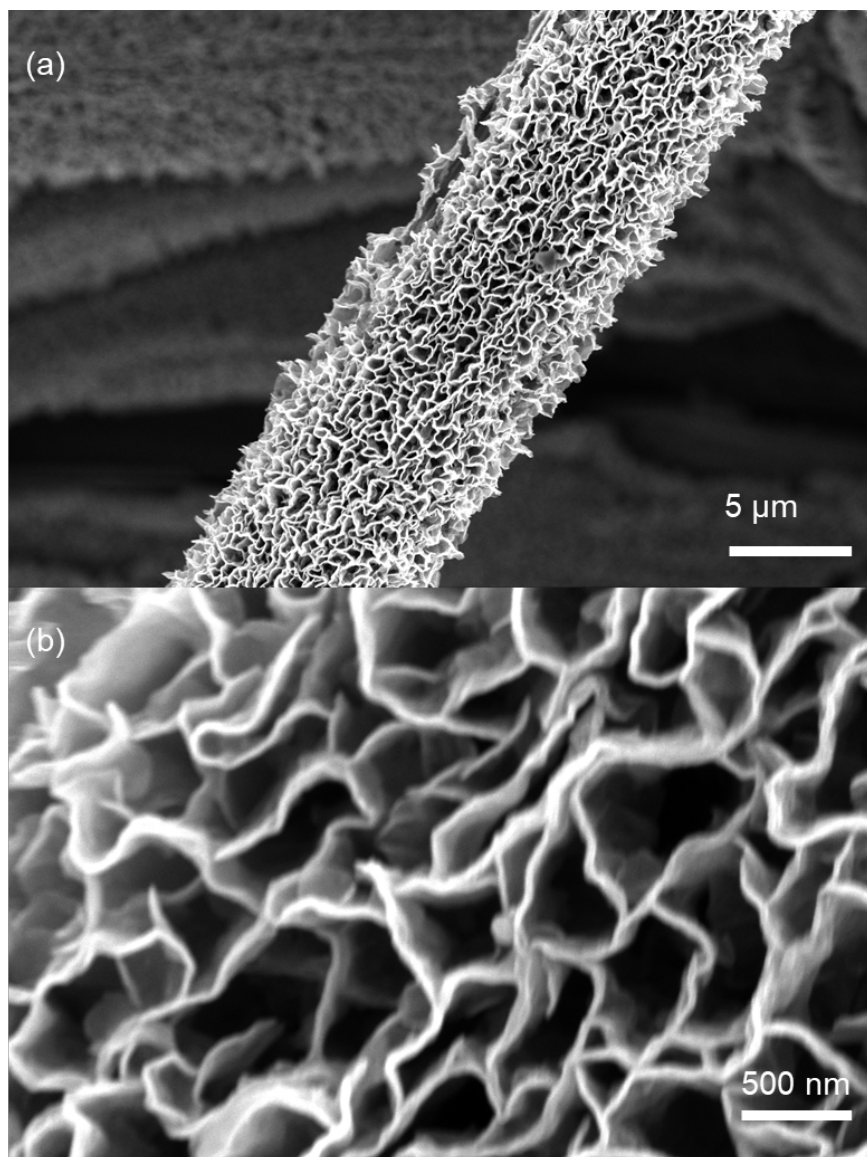


Figure S21. SEM images of CoN₄/VG electrode after 36 h production test in acidic media at different magnification (a and b).

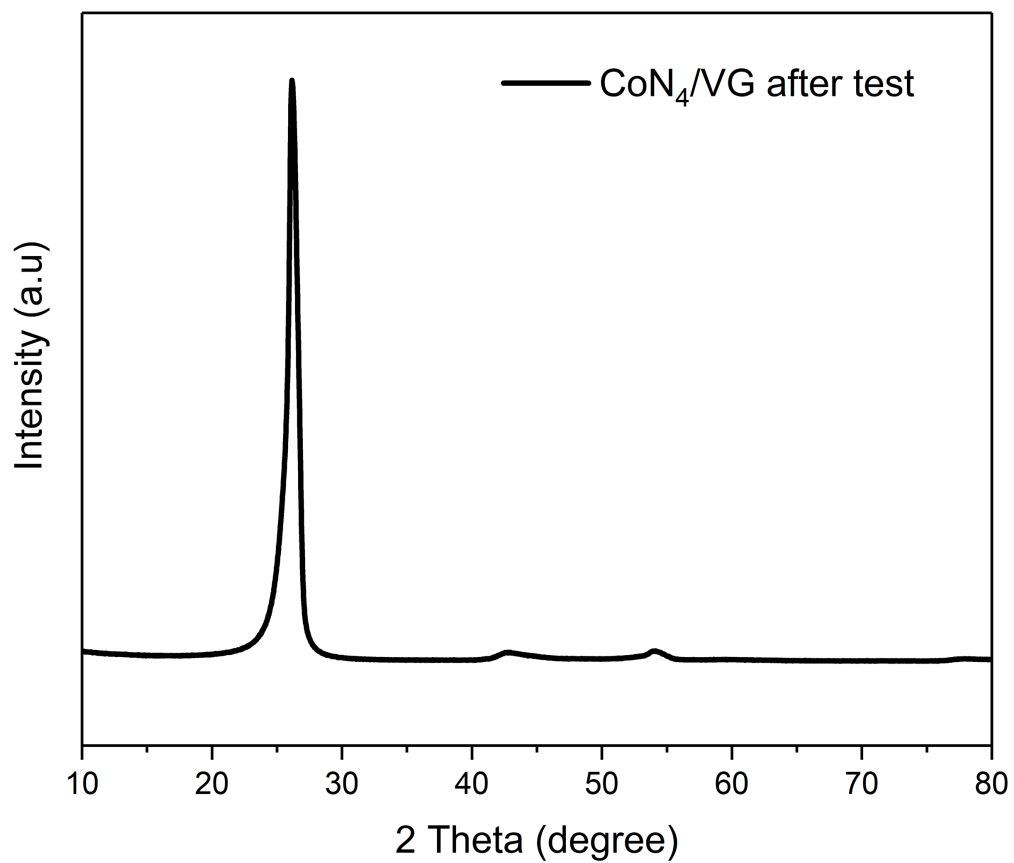


Figure S22. XRD pattern of CoN₄/VG electrode after 36 h cycling test in 0.1 M HClO₄ electrolyte.

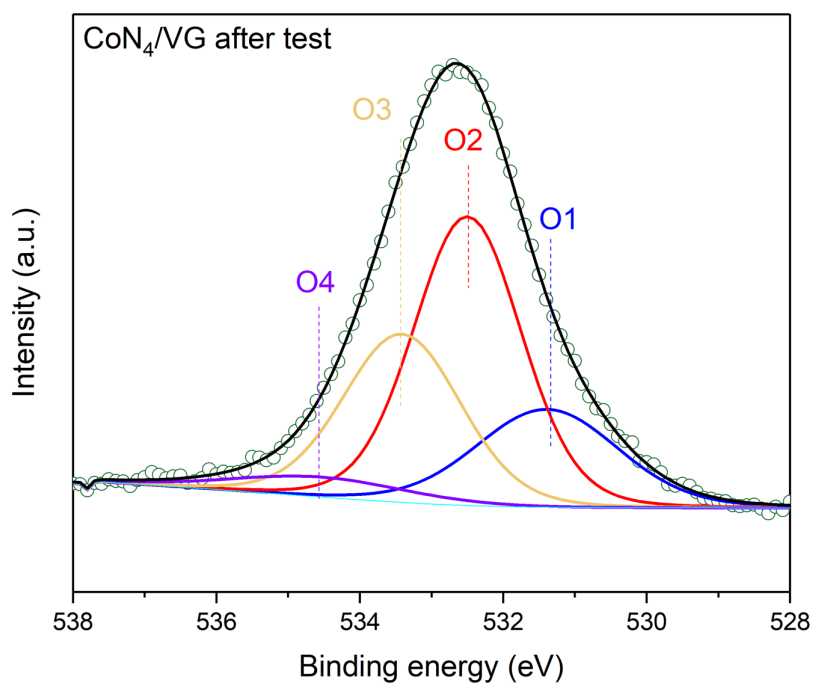


Figure S23. XPS O 1s spectra of CoN₄/VG electrode after 36 h cycling test in 0.1 M HClO₄ electrolyte, showing minor changes of the oxygen species that are beneficial for 2e⁻ ORR, as compared with that before test. (ketonic oxygen (C=O, O1, ~531.2eV), oxygen atoms in epoxy (C–O–C) or hydroxyl groups and carbonyl oxygen in ester groups (O2, ~532.3eV), the epoxy oxygen in ester groups (O3, ~533.5 eV), and oxygen atoms in carboxyl groups (O4, ~534.2eV)).

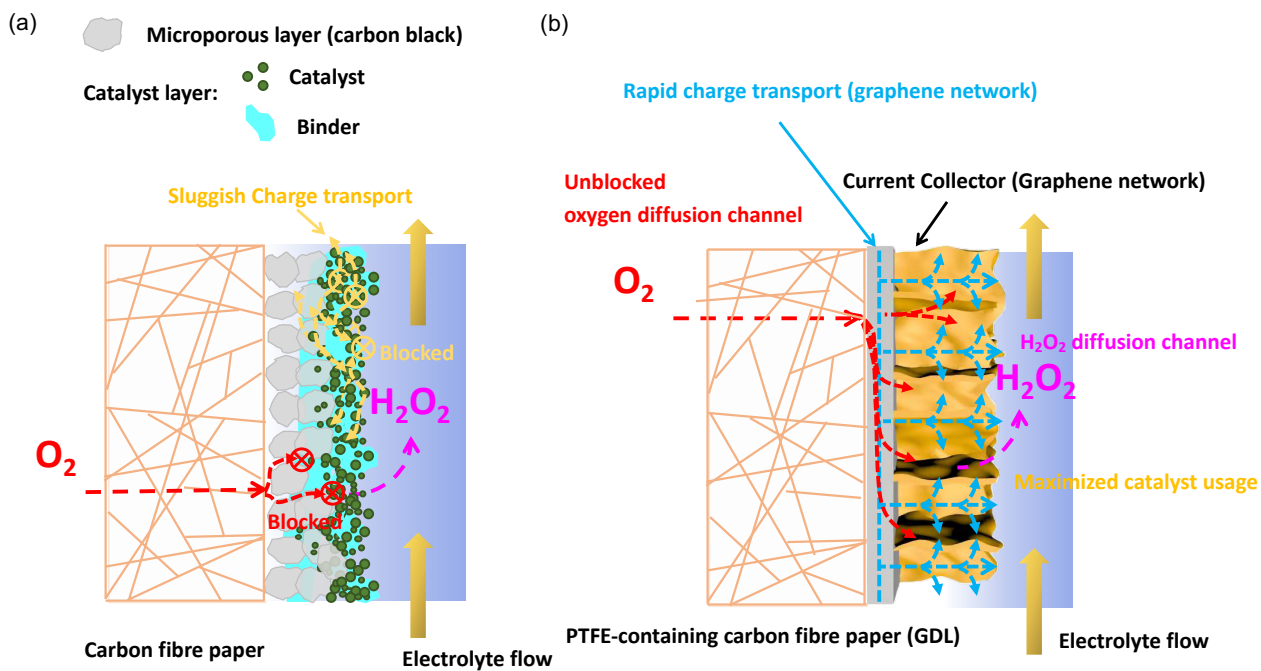


Figure S24. Schematic illustration of the conventional GDE setup (a), and the CoN₄/VG gas-diffusion electrode (b). The gas diffusion layer of the latter can be constructed by treating the carbon fibre paper with PTFE (See detailed electrode treatments in this document).

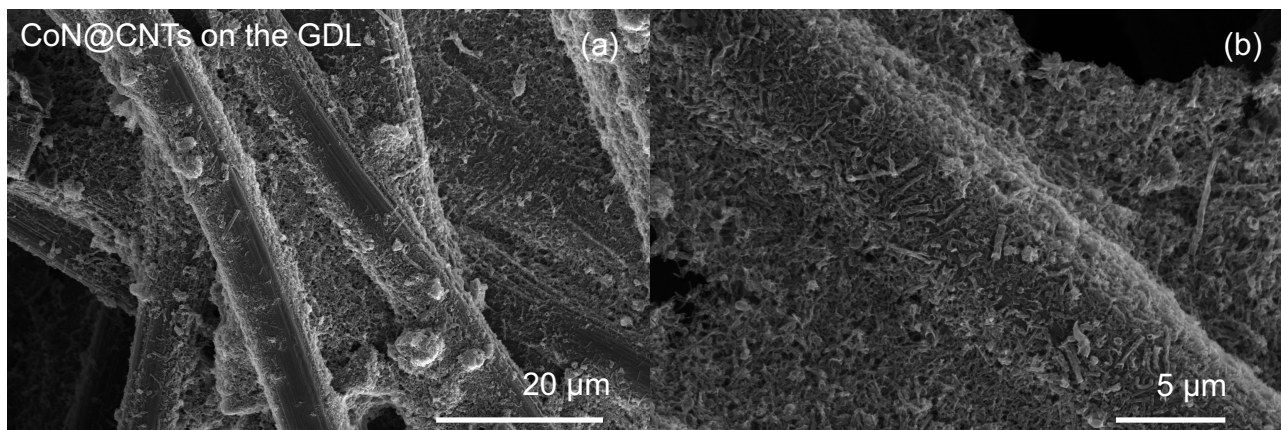


Figure S25. SEM images of the CoN@CNTs GDE, prepared by the drop-casting technique at different magnifications (a and b).

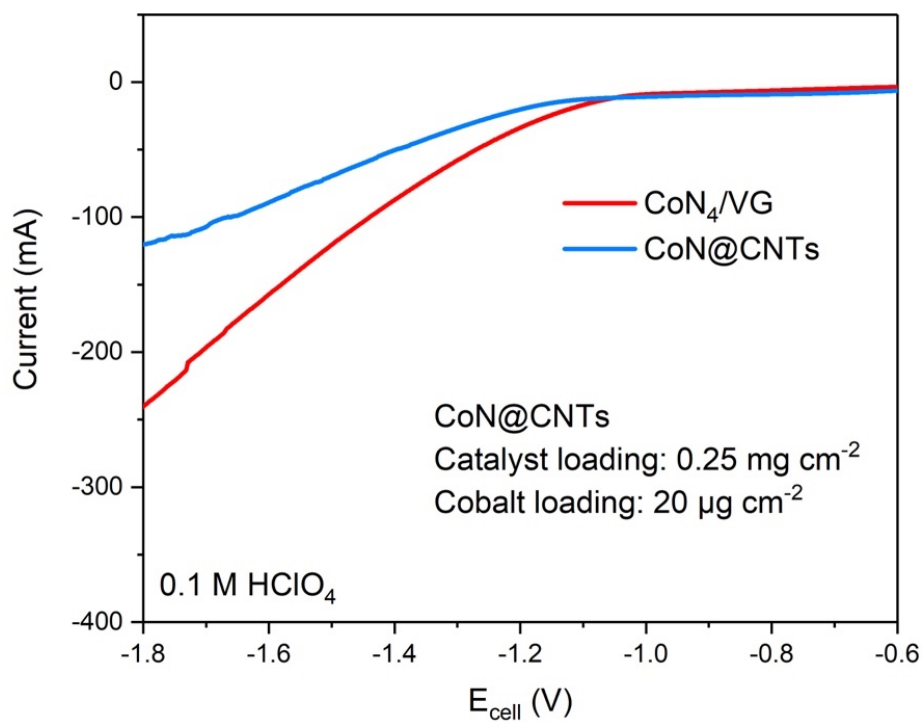


Figure S26. Linear sweep voltammetry (LSV) curves of the CoN₄/VG electrode and the CoN@CNTs electrode in flow cell utilizing O₂ at a scan rate of 5 mV s⁻¹.

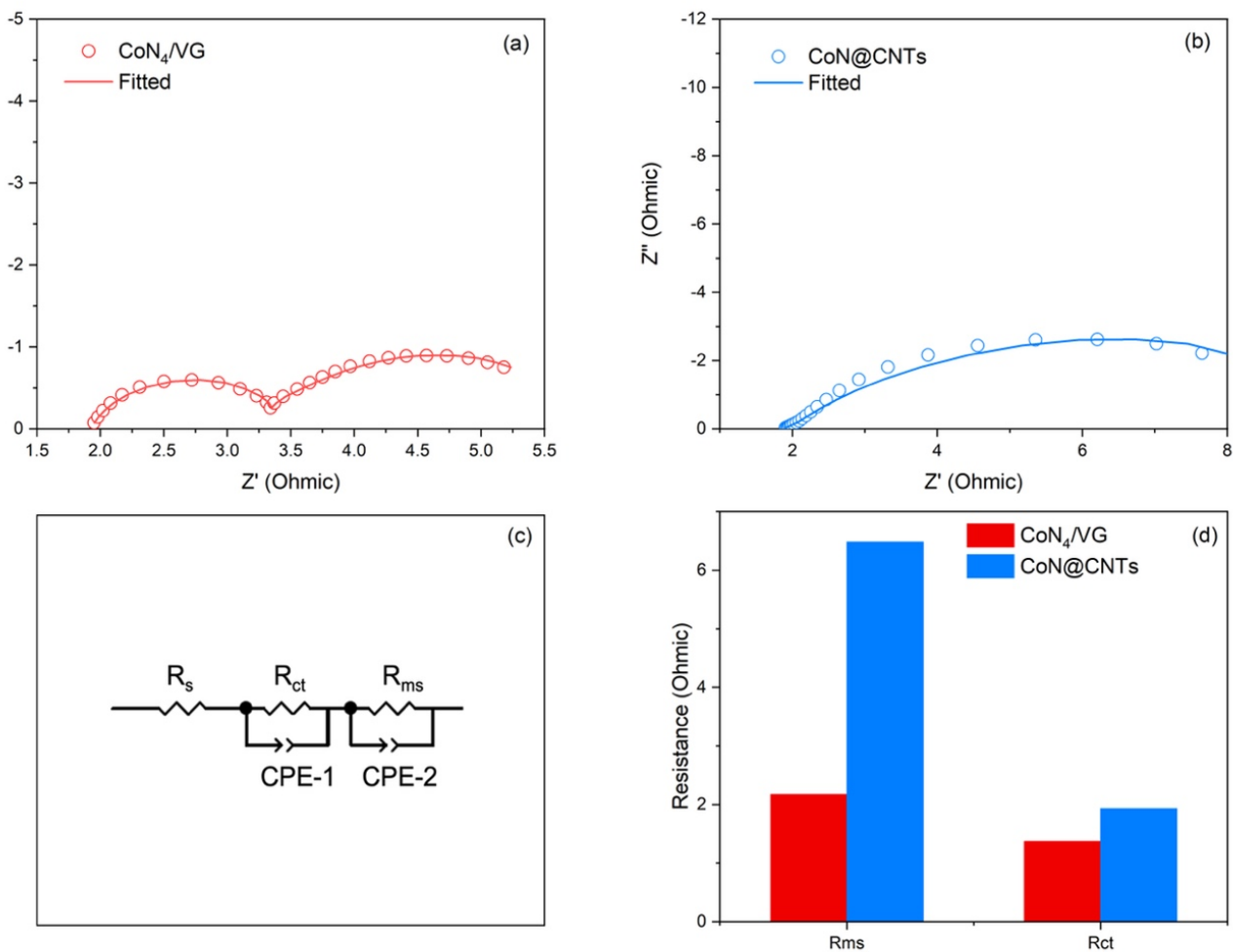


Figure S27. Nyquist plots of flow cell system obtained with CoN₄/VG GDE (a) and CoN@CNTs GDE (b) during ORR conditions in 0.1 M HClO₄ at a frequency range of $10^5 - 10^{-1}$ Hz, the proposed equivalent circuit to describe the electrochemical process (c), and the obtained results of charge transfer (R_{ct}) and the mass transfer (R_{ms}) resistance by fitting.

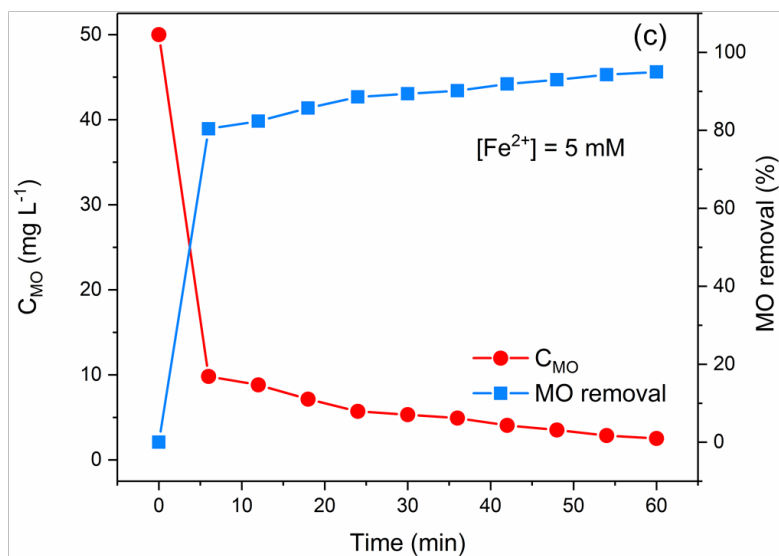
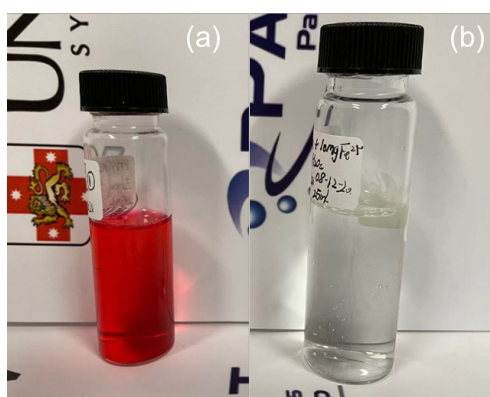


Figure S28. Digital photos of solution electrolytes containing the pollutant before (a) and after 1h degradation (b); degradation of 50 mg L⁻¹ MO over time monitored by UV-VIS in the presence of 5 mM Fe²⁺ and 1100 ppm H₂O₂ (c).

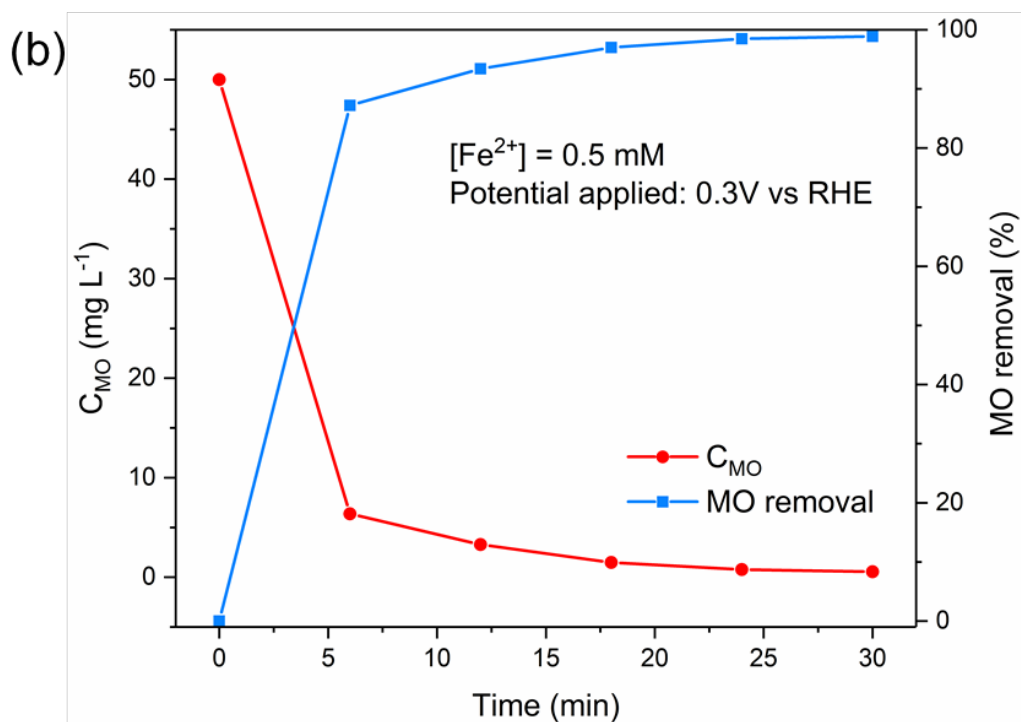
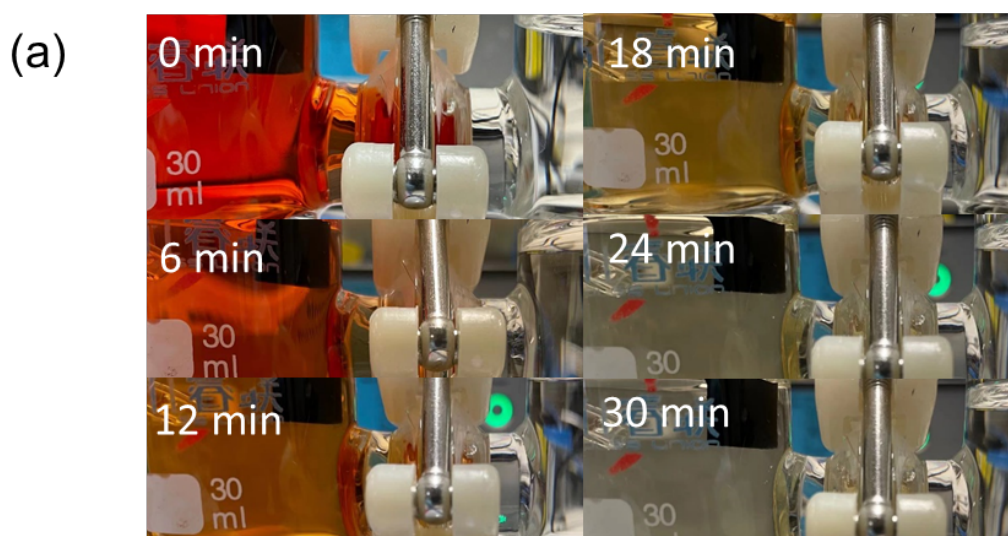


Figure S29. Digital photos showing colour evolution of solution electrolytes during 30 min degradation using CoN₄/ VG as working electrode applying 0.3 V vs RHE in the presence of 5 mM Fe²⁺ and 1100 ppm H₂O₂ (a); concentration evolution of MO over time monitored by UV-VIS, with initial concentration of 50 mg L⁻¹ (b).

Table S1. Metal compositions of CoN₄/VG electrode and CoN₄/VG electrode from ICP.

Samples	Metal content ($\mu\text{g cm}_{\text{electrode}}^{-2}$)
CoN ₄ /VG prior to acid wash	18.9
Resultant CoN ₄ /VG	4.2
Resultant CoN ₄ /CP	1.01

Table S2. Fitting parameters for Co K-edge EXAFS spectrum of CoN₄/VG electrode.

Samples	Absorption edge	Path	R (\AA)	CN	σ^2 (\AA^2)	R factor
CoN ₄ /VG	Co K-edge	Co-N	1.98650(0.02429)	4.05(1.14)	0.002(0.00003)	0.01493

CN is the coordination number; R is interatomic distance between metal center and first neighbor atoms; σ^2 is Debye-Waller factor which aims to compensate thermal and static disorder in the absorber-scatter distance; R factor is used to evaluate the correctness of fitting.

Table S3. Comparison of our electrode with the recent state-of-the-art counterparts for acidic H₂O₂ production via 2e⁻ ORR reaction in H-cell.

Samples	Electrolyte	H ₂ O ₂ Faradaic efficiency			Presented stability duration	Reference
		0.3 V vs RHE	0.4 V vs RHE	0.5 V vs RHE		
CoN ₄ /VG	0.1 M HClO ₄	97.7%	95.5%	92.3%	36h	This work
CoN@CNT	0.1 M HClO ₄	~88%	N/A	~90 %	12h	16
Co-N-C (1)	0.5 M H ₂ SO ₄	~60%	N/A	~40%	6h	20
Co-N-C (2)	0.1 M HClO ₄	N/A	~80%	~84%	10h	36
CoS ₂	0.05 M H ₂ SO ₄	N/A	N/A	~43%	1h	37
NiS ₂	0.05 M H ₂ SO ₄	~75%	~85%	~80%	6.67h	38
o-CoSe ₂ /CFP	0.05 M H ₂ SO ₄	N/A	N/A	~70%	6h	39
PEI50CMK3_800T (N-C (1))	0.5 M H ₂ SO ₄	~45%	N/A	N/A	4h	40
NCMK3IL50_800T (N-C (2))	0.5 M H ₂ SO ₄	72.5%	N/A	N/A	6h	41
g-N-CNHS (N-C (3))	0.1 M HClO ₄	~100%	N/A	N/A	24h	42
Pt/Hg	0.1 M HClO ₄	N/A	~80%	N/A	N/A	43
HPC-H24 (N-C (4))	0.5 M H ₂ SO ₄	90.8%	N/A	N/A	2.5h	18

Table S4. Comparison of productivity using our electrode and the recent state-of-the-art counterparts for acidic H₂O₂ production via 2e⁻ ORR reaction in H-cell.

Samples	Electrolyte	Maximized productivity	Reference
CoN ₄ /VG	0.1 M HClO ₄	706 mmol g _{catalyst} ⁻¹ h ⁻¹ (13576 mmol g _{Co} ⁻¹ h ⁻¹ /0.0537 mmol cm ⁻² h ⁻¹) at 0.3 V _{RHE}	This work
h-Pt ₁ -CuS _x	0.1 M HClO ₄	546 mmol g _{catalyst} ⁻¹ h ⁻¹ (899 mmol g _{Pt} ⁻¹ h ⁻¹) at 0.05 V (cell voltage, hydrogen oxidation as anode reaction)	44
Pt/HSC	1 M HClO ₄	48.75 mmol g _{catalyst} ⁻¹ h ⁻¹ at 0 V (cell voltage, hydrogen oxidation as anode reaction)	45
Co-N-C (1)	0.5 M H ₂ SO ₄	90.9 mmol g _{catalyst} ⁻¹ h ⁻¹ (9090 mmol g _{Co} ⁻¹ h ⁻¹) at 0.1 V _{RHE}	20
Co-N-C (2)	0.1 M HClO ₄	275 mmol g _{catalyst} ⁻¹ h ⁻¹ (19642 mmol g _{Co} ⁻¹ h ⁻¹) at 0.4 V _{RHE}	36
CoNOC	0.1 M HClO ₄	590 mmol g _{catalyst} ⁻¹ h ⁻¹ (295000 mmol g _{Co} ⁻¹ h ⁻¹ /0.118 mmol cm ⁻² h ⁻¹) at 0.1 V _{RHE}	46
PEI50CMK3_800T (N-C (1))	0.5 M H ₂ SO ₄	98 mmol g _{catalyst} ⁻¹ h ⁻¹ at 0.1 V _{RHE}	40
NCMK3IL50_800T (N-C (2))	0.5 M H ₂ SO ₄	157 mmol g _{catalyst} ⁻¹ h ⁻¹ at 0.1 V _{RHE}	41
HPC-H24 (N-C (4))	0.5 M H ₂ SO ₄	294 mmol g _{catalyst} ⁻¹ h ⁻¹ at 0 V _{RHE}	18
meso-BMP-800(N-C (5))	0.1 M HClO ₄	121.5 mmol g _{catalyst} ⁻¹ h ⁻¹ at 0.1 V _{RHE}	47

o-CoSe₂/CFP 0.05 M 7.65 mmol g_{catalyst}⁻¹ h⁻¹ (29.42 mmol g_{Co}⁻¹ h⁻¹) 39
H₂SO₄ at 0.5 V_{RHE}

Table S5. Comparison of Turnover frequency (TOF) and Turnover number (TON) of our catalyst electrode and the recent state-of-the-art counterparts for acidic H₂O₂ production via 2e⁻ ORR reaction in H-cell.

Samples	TOF	TON	Reference
CoN ₄ /VG	1045 h ⁻¹ (0.3 V _{RHE})	6270 (6 h at 0.3 V _{RHE})	This work
h-Pt ₁ -CuS _x	457 h ⁻¹ (cell voltage of 0.05V)	457 (cell voltage of 0.05V, 1h)	44
Co-N-C (1)	863 h ⁻¹ (0.1 V _{RHE})	3456 (4 h)	20
o-CoSe ₂ /CFP	2.47 h ⁻¹ (0.5 V _{RHE})	14.86 (6 h at 0.4V _{RHE})	39
CoN@CNT	5.30 h ⁻¹ (0.45 V _{RHE})	63.6 (12 h at 0.45V _{RHE})	16
CoS ₂	3.15 (0.5 V _{RHE})	3.15 (1 h at 0.5 V _{RHE})	37

Table S6. Metal compositions (cobalt) of electrolyte sampled from electrolysis test (ICP results, H-cell and flow cell).

Samples	Metal content ($\mu\text{g L}^{-1}$ electrolyte⁻¹)
Electrolyte from H-cell test (6h)	17.6
Electrolyte from flow cell test (1h)	4.01
Electrolyte from flow cell test (6h)	3.48
Pristine electrolyte	Below detection limit
MDL	0.10

MDL-Method detection limit is the lowest concentration at which an analyte can be detected in a sample with 99% certainty.

Table S7. Selected two-electrode cell systems reported for electrosynthesis of acidic H₂O₂.

Cell configuration and setup	Operation condition		[H ₂ O ₂]	Faradaic efficiency	Production rate	Energy consumption	Reference
	Electrolyte	Potential/ current					
Two-electrode pre-pilot plant, 20cm ² Ti RuO ₂ -based anode, a 20cm ² CoS _x P _y /MWC NT air-diffusion cathode (catalyst loading: 2.0 mg cm ⁻²)	2.5 L of 0.05M Na ₂ SO ₄ , pH=3	5V, 200 mA	136 ppm	60% (6h)	0.094 mmol cm ⁻² h ⁻¹ /47 mmol g _{catalyst} ⁻¹ h ⁻¹	17.6 Wh g ⁻¹	48
		9-10V, 500 mA	408 ppm	60% (6h)	0.25 mmol cm ⁻² h ⁻¹ /125 mmol g _{catalyst} ⁻¹ h ⁻¹	27.9 Wh g ⁻¹	
		13-14V, 800 mA	510 ppm	60% (6h)	0.315 mmol cm ⁻² h ⁻¹ /156 mmol g _{catalyst} ⁻¹ h ⁻¹	50.8 Wh g ⁻¹	
Two-electrode flow cell, 17cm ² Ti RuO ₂ -based anode, a 180cm ² reticulated vitreous carbon cathode	2 L of 0.05M Na ₂ SO ₄ , pH=3	3.2 V, 59.5 mA	14 ppm	30% (3h)	0.0015 mmol cm ⁻² h ⁻¹	20.4 Wh g ⁻¹	49
		4.5 V, 119 mA	13 ppm	18% (3h)	0.0014 mmol cm ⁻² h ⁻¹	61.7 Wh g ⁻¹	
		6.0 V, 178.5 mA	11 ppm	9% (3h)	0.0012 mmol cm ⁻² h ⁻¹	153 Wh g ⁻¹	
Two-electrode Cylindrical cell, cylindrical Pt gauze anode, a 4 cm ² carbon sponge cathode	0.125 L of 0.05M Na ₂ SO ₄ , pH=3 (20 °C)	4.3 V, 100 mA	272 ppm	21% (2.5h)	0.1 mmol cm ⁻² h ⁻¹	31.6 Wh g ⁻¹	50
Two-electrode flow cell, a RuO ₂ -based Co SA/CC cathode	0.1 M HClO ₄	~1.65 V, 25 mA	1840 ppm	N/A	675 mmol g _{catalyst} ⁻¹ h ⁻¹	N/A	51

Two-electrode flow reactor, a MMO anode, carbon black/activated carbon polyvinylidene fluoride (CB/AC/PVDF) cathode (catalyst loading :20 mg cm ⁻²)	40 mL 0.1M Na ₂ SO ₄	1.8 V, 38 mA (10 cm ² cathode)	182 ppm	30.2% (1h)	0.02 mmol cm ⁻² h ⁻¹	8.0 Wh g ⁻¹	52
	200 mL 0.1M Na ₂ SO ₄	1.8 V, 160 mA (79 cm ² cathode)	210 ppm	49.2% (1h)	0.0186 mmol cm ⁻² h ⁻¹	5.4 Wh g ⁻¹	
	3L 0.1M Na ₂ SO ₄	1.8 V, 600 mA (707 cm ² cathode)	66 ppm	53% (1h)	0.008 mmol cm ⁻² h ⁻¹	4.9 Wh g ⁻¹	
Two-electrode Cylindrical cell, a Pt screen anode, a 20cm ² cobalt (II) phthalocyanine (CoPc) based gas diffusion electrode	400 mL electrolyte containing g H ₂ SO ₄ (0.1 mol L ⁻¹) and K ₂ SO ₄ (0.1 mol L ⁻¹).	3.45 V, 270 mA	90 ppm	14% (90 min)	0.041 mmol cm ⁻² h ⁻¹	38.8 Wh g ⁻¹	53
		4.54 V, 880 mA	300 ppm	20% (90 min)	0.165 mmol cm ⁻² h ⁻¹	50 Wh g ⁻¹	
Two-electrode flow cell, 100cm ² DSA anode and a 100cm ² carbon-PTFE GDE cathode	5 L of 0.05M Na ₂ SO ₄ , pH=3	7.5V, 5A	468 ppm	73.7% (1h)	0.688 mmol cm ⁻² h ⁻¹	16.02 Wh g ⁻¹	54
Two-electrode flow cell, a 100cm ² carbon-GDE cathode	pH=3, 25L	3A	20 ppm	51.7%	0.294 mmol cm ⁻² h ⁻¹	N/A	55
Two-electrode flow cell, a DSA anode, 10 cm ² CoN ₄ /VG gas diffusion electrode (catalyst loading: 0.076 mg cm ⁻²)	540 mL of 0.1 M HClO ₄ (6 h)	1.8 V, ~210 mA	1100 ppm	70% (6h)	0.304 mmol cm ⁻² h ⁻¹ / 4001 mmol g _{catalyst} ⁻¹ h ⁻¹	3.81 Wh g ⁻¹	This work

Table S8. Comparison of Turnover frequency (TOF) and Turnover number (TON) of our catalyst electrode and the recent state-of-the-art counterparts for acidic H₂O₂ production via 2e⁻ ORR reaction in 2-electrode cell application.

Samples	Cell voltage or current	TOF	TON	Reference
CoN ₄ /VG gas diffusion electrode	1.8 V (~240 mA)	5757 h ⁻¹	34542 (6h)	This work
CoS _x P _y /MWCNT	5 V	20.35 h ⁻¹	122 (6h)	
air-diffusion cathode	9-10 V	50.88 h ⁻¹	305.28 (6h)	48
	13-14 V	81.42 h ⁻¹	488.52 (6h)	
Co SA/CC cathode	25 mA	2291 h ⁻¹	9166 (4 h)	51

Reference

1. Z. Ma, C. Tsounis, P. V. Kumar, Z. Han, R. J. Wong, C. Y. Toe, S. Zhou, N. M. Bedford, L. Thomsen, Y. H. Ng and R. Amal, *Advanced Functional Materials*, 2020, **30**, 1910118.
2. C. Tsounis, X. Lu, N. M. Bedford, B. Subhash, L. Thomsen, Q. Zhang, Z. Ma, K. Ostrikov, A. Bendavid and J. A. Scott, *ACS Nano*, 2020, **14**, 11327-11340.
3. M. R. Haider, W.-L. Jiang, J.-L. Han, H. M. A. Sharif, Y.-C. Ding, H.-Y. Cheng and A.-J. Wang, *Applied Catalysis B: Environmental*, 2019, **256**, 117774.
4. Y. P. Zhu, Y. Jing, A. Vasileff, T. Heine and S.-Z. Qiao, *Advanced Energy Materials*, 2017, **7**.
5. X. Lu and C. Zhao, *Nature Communications*, 2015, **6**, 1-7.
6. Y. Zhong, Y. Lu, Z. Pan, J. Yang, G. Du, J. Chen, Q. Zhang, H. Zhou, J. Wang and C. Wang, *Advanced Functional Materials*, 2021, **31**, 2009853.
7. C. Guan, A. Sumboja, H. Wu, W. Ren, X. Liu, H. Zhang, Z. Liu, C. Cheng, S. J. Pennycook and J. Wang, *Advanced Materials*, 2017, **29**, 1704117.
8. L. Wang, Y. Wu, R. Cao, L. Ren, M. Chen, X. Feng, J. Zhou and B. Wang, *ACS Applied Materials & Interfaces*, 2016, **8**, 16736-16743.
9. Z. Zhang, W. Li, M. F. Yuen, T.-W. Ng, Y. Tang, C.-S. Lee, X. Chen and W. Zhang, *Nano Energy*, 2015, **18**, 196-204.
10. D. Xie, X. Xia, Y. Zhong, Y. Wang, D. Wang, X. Wang and J. Tu, *Advanced Energy Materials*, 2017, **7**, 1601804.
11. C. T. Dinh, T. Burdyny, M. G. Kibria, A. Seifitokaldani, C. M. Gabardo, F. P. Garcia de Arquer, A. Kiani, J. P. Edwards, P. De Luna, O. S. Bushuyev, C. Zou, R. Quintero-Bermudez, Y. Pang, D. Sinton and E. H. Sargent, *Science*, 2018, **360**, 783-787.

12. F. P. Garcia de Arquer, C. T. Dinh, A. Ozden, J. Wicks, C. McCallum, A. R. Kirmani, D. H. Nam, C. Gabardo, A. Seifitokaldani, X. Wang, Y. C. Li, F. Li, J. Edwards, L. J. Richter, S. J. Thorpe, D. Sinton and E. H. Sargent, *Science*, 2020, **367**, 661-666.
13. Z. Lu, W. Xu, J. Ma, Y. Li, X. Sun and L. Jiang, *Advanced Materials*, 2016, **28**, 7155-7161.
14. H. Zhang, Y. Zhao, Y. Li, G. Li, J. Li and F. Zhang, *ACS Applied Energy Materials*, 2019, **3**, 705-714.
15. Y. Li, H. Zhang, N. Han, Y. Kuang, J. Liu, W. Liu, H. Duan and X. Sun, *Nano Research*, 2019, **12**, 177-182.
16. Q. Zhang, X. Tan, N. M. Bedford, Z. Han, L. Thomsen, S. Smith, R. Amal and X. Lu, *Nature Communications*, 2020, **11**, 4181.
17. V. Čolić, S. Yang, Z. Révay, I. E. L. Stephens and I. Chorkendorff, *Electrochimica Acta*, 2018, **272**, 192-202.
18. Y. Liu, X. Quan, X. Fan, H. Wang and S. Chen, *Angewandte Chemie International Edition*, 2015, **54**, 6837-6841.
19. I. Yamanaka and T. Murayama, *Angewandte Chemie International Edition*, 2008, **47**, 1900-1902.
20. Y. Sun, L. Silvioli, N. R. Sahraie, W. Ju, J. Li, A. Zitolo, S. Li, A. Bagger, L. Arnarson, X. Wang, T. Moeller, D. Bernsmeier, J. Rossmeisl, F. Jaouen and P. Strasser, *Journal of the American Chemical Society*, 2019, **141**, 12372-12381.
21. Q. Zhao, Y. Wang, W.-H. Lai, F. Xiao, Y. Lyu, C. Liao and M. Shao, *Energy & Environmental Science*, 2021, **14**, 5444-5456.
22. Y. Zhong, Z. Pan, X. Wang, J. Yang, Y. Qiu, S. Xu, Y. Lu, Q. Huang and W. Li, *Advanced*

- Science*, 2019, **6**, 1802243.
23. Y. Zhong, Y. Lu, Z. Pan, J. Yang, G. Du, J. Chen, Q. Zhang, H. Zhou, J. Wang and C. Wang, *Advanced Functional Materials*, 2021, **31**, 2009853.
 24. C. Guan, A. Sumboja, W. Zang, Y. Qian, H. Zhang, X. Liu, Z. Liu, D. Zhao, S. J. Pennycook and J. Wang, *Energy Storage Materials*, 2019, **16**, 243-250.
 25. Z. Li, J. Yang, X. Ge, Y.-P. Deng, G. Jiang, H. Li, G. Sun, W. Liu, Y. Zheng and H. Dou, *Nano Energy*, 2021, **89**, 106314.
 26. E. Brillas, I. Sirés and M. A. Oturan, *Chemical Reviews*, 2009, **109**, 6570-6631.
 27. A. J. Bard and L. R. Faulkner. *Electrochemical methods: Fundamentals and applications 2nd Edition*. John Wiley & Sons, Inc, New York, 2001.
 28. Z. Lu, G. Chen, S. Siahrostami, Z. Chen, K. Liu, J. Xie, L. Liao, T. Wu, D. Lin, Y. Liu, T. F. Jaramillo, J. K. Nørskov and Y. Cui, *Nature Catalysis*, 2018, **1**, 156-162.
 29. H. W. Kim, M. B. Ross, N. Kornienko, L. Zhang, J. Guo, P. Yang and B. D. McCloskey, *Nature Catalysis*, 2018, **1**, 282-290.
 30. J. Zhang, Z. Xia and L. Dai, *Science Advances*, 2015, **1**, e1500564.
 31. J. L. Figueiredo, M. Pereira, M. Freitas and J. Orfao, *Carbon*, 1999, **37**, 1379-1389.
 32. H.-W. Liang, S. Brüller, R. Dong, J. Zhang, X. Feng and K. Müllen, *Nature Communications*, 2015, **6**, 1-8.
 33. X. Zhu, X. Tan, K.-H. Wu, C.-L. Chiang, Y.-C. Lin, Y.-G. Lin, D.-W. Wang, S. Smith, X. Lu and R. Amal, *Journal of Materials Chemistry A*, 2019, **7**, 14732-14742.
 34. K. Vijayarangamuthu, S. Ahn, H. Seo, S. H. Yoon, C. M. Park and K. J. Jeon, *Advanced Materials*, 2016, **28**, 661-667.

35. C. C. McCrory, S. Jung, J. C. Peters and T. F. Jaramillo, *Journal of the American Chemical Society*, 2013, **135**, 16977-16987.
36. J. Gao, H. b. Yang, X. Huang, S.-F. Hung, W. Cai, C. Jia, S. Miao, H. M. Chen, X. Yang, Y. Huang, T. Zhang and B. Liu, *Chem*, 2020, **6**, 658-674.
37. H. Sheng, E. D. Hermes, X. Yang, D. Ying, A. N. Janes, W. Li, J. R. Schmidt and S. Jin, *ACS Catalysis*, 2019, **9**, 8433-8442.
38. J. Liang, Y. Wang, Q. Liu, Y. Luo, T. S. Li, H. Zhao, S. Lu, F. Zhang, A. M. Asiri and F. Liu, *Journal of Materials Chemistry A*, 2021, **9**, 6117-6122.
39. H. Sheng, A. N. Janes, R. D. Ross, D. Kaiman, J. Huang, B. Song, J. R. Schmidt and S. Jin, *Energy & Environmental Science*, 2020, **13**, 4189-4203.
40. Y. Sun, S. Li, Z. P. Jovanov, D. Bernsmeier, H. Wang, B. Paul, X. Wang, S. Kuhl and P. Strasser, *ChemSusChem*, 2018, **11**, 3388-3395.
41. Y. Sun, I. Sinev, W. Ju, A. Bergmann, S. Dresch, S. Kühn, C. Spöri, H. Schmies, H. Wang, D. Bernsmeier, B. Paul, R. Schmack, R. Kraehnert, B. Roldan Cuenya and P. Strasser, *ACS Catalysis*, 2018, **8**, 2844-2856.
42. D. Iglesias, A. Giuliani, M. Melchionna, S. Marchesan, A. Criado, L. Nasi, M. Bevilacqua, C. Tavagnacco, F. Vizza, M. Prato and P. Fornasiero, *Chem*, 2018, **4**, 106-123.
43. S. Siahrostami, A. Verdaguer-Casadevall, M. Karamad, D. Deiana, P. Malacrida, B. Wickman, M. Escudero-Escribano, E. A. Paoli, R. Frydendal, T. W. Hansen, I. Chorkendorff, I. E. Stephens and J. Rossmeisl, *Nature Materials*, 2013, **12**, 1137-1143.
44. R. Shen, W. Chen, Q. Peng, S. Lu, L. Zheng, X. Cao, Y. Wang, W. Zhu, J. Zhang, Z. Zhuang, C. Chen, D. Wang and Y. Li, *Chem*, 2019, **5**, 2099-2110.

45. C. H. Choi, M. Kim, H. C. Kwon, S. J. Cho, S. Yun, H.-T. Kim, K. J. Mayrhofer, H. Kim and M. Choi, *Nature Communications*, 2016, **7**, 1-9.
46. C. Tang, L. Chen, H. Li, L. Li, Y. Jiao, Y. Zheng, H. Xu, K. Davey and S. Z. Qiao, *Journal of the American Chemical Society*, 2021, **143**, 7819-7827.
47. T. P. Fellingner, F. Hasche, P. Strasser and M. Antonietti, *Journal of the American Chemical Society*, 2012, **134**, 4072-4075.
48. Z. Ye, D. R. V. Guelfi, G. Álvarez, F. Alcaide, E. Brillas and I. Sirés, *Applied Catalysis B: Environmental*, 2019, **247**, 191-199.
49. O. M. Cornejo, I. Sirés and J. L. Nava, *Journal of Electroanalytical Chemistry*, 2020, **873**, 114419.
50. A. Özcan, Y. Şahin, A. Savaş Kopalal and M. A. Oturan, *Journal of Electroanalytical Chemistry*, 2008, **616**, 71-78.
51. J. Zhang, H. Yang, J. Gao, S. Xi, W. Cai, J. Zhang, P. Cui and B. Liu, *Carbon Energy*, 2020, **2**, 276-282.
52. H. Zhang, Y. Li, G. Li and F. Zhang, *Electrochimica Acta*, 2019, **299**, 273-280.
53. W. R. P. Barros, R. M. Reis, R. S. Rocha and M. R. V. Lanza, *Electrochimica Acta*, 2013, **104**, 12-18.
54. G. R. Agladze, G. S. Tsurtsunia, B. I. Jung, J. S. Kim and G. Gorelishvili, *Journal of Applied Electrochemistry*, 2007, **37**, 375-383.
55. I. Salmerón, K. V. Plakas, I. Sirés, I. Oller, M. I. Maldonado, A. J. Karabelas and S. Malato, *Applied Catalysis B: Environmental*, 2019, **242**, 327-336.